

**Depth Assessment**  
**in 2D Planar-Scanning Diffuse Optical Imaging**

A thesis submitted by  
**Roni Cantor-Balan**

In partial fulfillment of the requirements

for the degree of

**Master of Science**

in

*BIOMEDICAL ENGINEERING*

**TUFTS UNIVERSITY**

May 2013

ADVISER:

Sergio Fantini, Ph.D., Department of Biomedical Engineering, Tufts University

Committee Members:

Irene Georgakoudi , Ph.D., Department of Biomedical Engineering, Tufts University

Misha Kilmer, Ph.D., Department of Mathematics, Tufts University

## Abstract

Methods for depth assessment in planar-scanning diffuse optical imaging have been recently proposed for the purpose of advancing optical mammography. The typical 2D planar-scanner includes a collinear source-detector pair that scans the breast in the x-y plane and provides a 2D projection image. A second optical detector that is off-axis with respect to the light source has been introduced to determine the depth of a detected object from its spatial shift between the on-axis and off-axis images. The spatial shift of the object was associated to its depth through a theoretical depth-shift curve obtained with diffusion theory. The theoretical depth-shift curve has been shown to be insensitive to variations in sample thickness, background optical properties and inclusion size. In this study, we have experimentally measured depth-shift curves to verify such insensitivity and to confirm the validity of the theoretical predictions under practical experimental conditions that do not match the ideal conditions used to derive the theoretical depth-shift curves. We have experimentally confirmed the insensitivity of the depth-shift curve to sample thickness, inclusion size, and background optical properties for absorption coefficients  $> 0.09 \text{ cm}^{-1}$ . For lower values of the background absorption coefficient, the experimental depth-shift curves deviate from the reported theoretical curves resulting in depth assessment differences of 3-7 mm. We assign this discrepancy to the effect of experimental boundary conditions, which becomes more significant at low absorption values for which the optically probed volume becomes larger. Considering the low absorption coefficient of breast tissue in the near-infrared region (typically  $\sim 0.05 \text{ cm}^{-1}$ ), the results of this thesis indicate that it is appropriate to experimentally derive a depth-shift curve that is specific to the optical mammography system to be used.

## **Acknowledgments**

First and foremost, I would like to express my sincere gratitude to my advisor, Professor Sergio Fantini, for his guidance and engagement throughout the course of my studies. His scientific and logical approach is both impressive and inspiring. His leadership in the biomedical field helped overcome the obstacles in the completion of this research work. Working in his lab I have gained invaluable knowledge and have been exposed to the diffuse optics world in the most professional and fascinating way. I am confident in the set of tools he has provided me with and which creates an additional layer in my professional path.

I would like to convey my deepest appreciation to Professor Angelo Sassaroli for his invaluable teaching and advice in the past two years. His wisdom in the diffuse optics field together with his patience and willingness to share his knowledge have provided me with a deeper understanding of the discipline as well as enhanced my foundation for approaching engineering problems. Along with our scientific discussions I greatly enjoyed our conversations about family, culture and life in general.

I would like to express my special thanks to Professor Irene Georgakoudi who has given me the opportunity to work in her lab prior to my formal joining to the graduate program. Conducting research under her guidance has laid a firm foundation for my studies and has equipped me with valuable knowledge in the biomedical optics field.

Special thanks are dedicated to Jana Kainerstorfer, our knowledgeable postdoctoral who has provided me with both professional and personal support throughout the entire process. Her wonderful articulating capabilities together with her profound knowledge in optics have been priceless in countless situations.

I would like to thank Pami Anderson and Lia Hocke, lab mates and dear friends who have made this experience pleasant with their graceful characters, support and fun discussions about anything but optics. I would also like to thank my lab mates Gee Weliwitigoda, Bertan Hallacoglu and Michele Pierro for their kind advice and precious time in assisting me with my work. I cherish our conversations and greatly appreciate your support.

To my wonderful parents in law, Shoshi and Moshe Balan, I would like to express my deepest gratitude and love for their enormous support throughout my studies.

To my dear parents, Rachel and Udi Cantor, who have extended their unconditional love all the way from Israel and have supported me as they always do, I have not enough space in this report to express my gratitude and love to them both.

To my beloved husband Yoni, and to my baby boy Eytan, I would like to thank for being my guiding light and inspiration. Their presence in my life has made me a stronger person. Their love and support is in every step I take.

# Table of Contents

Chapter I – Introduction and Background.....	7
1.1 Introduction – The Role of Optical Methods in Breast Cancer Diagnosis.....	7
1.2 Background – Principals of Diffuse Optical Imaging.....	11
1.2.1 Light Interaction with Biological Tissue.....	11
1.2.2 Diffuse Optical Imaging.....	15
1.2.3 Optical Mammography Systems .....	17
1.2.4 The Diffusion Equation.....	18
1.2.5 Depth Discrimination in 2D Planar Scanning.....	22
Chapter II – Methods.....	27
2.1 Instrumentation for Measuring the Experimental Depth-Shift Curve.....	27
2.2 Data Acquisition.....	31
2.3 Raw Data Processing.....	33
2.3.1 Spatial Processing.....	33
2.3.2 Intensity Minima Identification.....	34
2.3.3 Generating the Depth-Shift Curve.....	37
2.4 Determining the depth-shift curve based on Diffusion Theory.....	38
Chapter III – Experiments and Protocols.....	38
3.1 Absolute Measurements of Background Optical Properties.....	38
3.1.1 Preparation of diluted India ink.....	39
3.1.2 Optical Properties Measurements of the Liquid Phantom.....	42
3.1.2.1 Experimental Setup.....	42

3.2.1.2 Data Analysis and Results.....	44
3.2 Variability of the Depth-Shift Curve.....	47
Chapter IV – Results.....	49
4.1 Sensitivity to Sample Thickness.....	49
4.2 Sensitivity to Background Optical Properties.....	53
4.3 Sensitivity to Inclusion Size.....	56
Chapter V – Discussion and Conclusions.....	59
References.....	65

# **Chapter I - Diffuse Optical Imaging - Introduction and Background**

## **1.1 Introduction – The Role of Optical Methods in Breast Cancer Diagnosis**

Breast cancer is the second leading cause of cancer deaths among women in the United States [Jemal et al, 2010]. In 2009, over two hundred thousand new cases were diagnosed in the U.S, leading to more than forty thousand deaths. Current projections of the American Cancer Society estimate that 1 in 8 women in the U.S will develop invasive breast cancer. Since 1990 breast cancer death rates in the U.S have been declining partly due to early detection and progress in treatment. The five-year survival rate for early diagnosis at a localized stage of the disease is 98% versus only 23% for later stages detection [Ries et al, 2007]. The encouraging numbers in survival rates due to early diagnosis together with the still high death rates are the motivation behind the growing research efforts for the prevention, detection and treatment of breast cancer.

The current gold standard tool for breast cancer screening is X-ray mammography. Although this method has been the dominating detection technique since the 1970s [Van Steen and Van Tiggelen, 2007] it has several limitations. For one, it introduces ionizing radiation into the body and although only small amounts are required, repeated x-rays increase the risk of developing cancer. For this reason x-ray mammograms cannot be used for continuous monitoring of treatment. Secondly, mammography is generally not applicable to women under the age of 40 due to high breast density. High false-negative (20%) and false-positive (50%) rates [Hubbard et al, 2011] are another major drawback. False-negative results, usually due to high breast density in younger women, can result in the delay of treatment, thus lowering the chances for survival. On the other hand, false-positive mammograms require further testing,

leading to stress and physical discomfort due to the high compression of the breast as well as yearly costs estimated at \$100 million [Cyrilak, 1998]. Other screening modalities, such as magnetic resonance imaging (MRI) and ultrasound serve as complimentary tools only, thus the need for an improved screening method still exists.

Diffuse optical imaging (DOI) is an emerging technology which can provide additional physiological information about breast tissue compared to the information acquired with X-ray. Since DOI uses near infrared (NIR) light, it has a penetration depth of several centimeters into the tissue and at the same time it is characterized as non-invasive. Its low cost implementation and use together with its health risk-free benefit make it an ideal tool for continuous monitoring of cancer treatment.

A specific application of DOI is known as optical mammography of the breast [Fantini and Sassaroli, 2012][Yu et al, 2009] [Enfield et al, 2007] [Grosenick et al, 2003, 2004]. At the basis of the method is the illumination and detection of NIR light that propagates through the breast tissue and which contains spectral information about the optical properties of the breast. Typically the desired information is the concentration of tissue chromophores which have been shown to differ between healthy and cancerous tissue [Grosenick et al, 2005] [Ntziachristos et al, 2002] [Yu et al, 2010]. Two of the main breast tumor characteristics are angiogenesis and hypoxia due to the increased demand of oxygen and nutrients at the tumor site. DOI is capable of providing a spatial oxygenation map of the breast based on the optical properties of NIR light in the tissue, thus enabling the identification of hypoxic and angiogenic areas which can be associated with breast cancer.

Although DOI is characterized by a high intrinsic contrast due to the absorption of light by hemoglobin, its spatial resolution is low (6-10 mm) [Pogue et al. 2006] because of the

diffusive nature of NIR light in the tissue. To improve the spatial resolution, 2D planar-scanning of the breast can be performed. [Grosenick et al, 2003] [Grosenicket al, 2004] [Yu et al, 2010]. In this method the breast is only slightly compressed between two parallel glass plates and a collinear source-detector pair in transmission mode scans the tissue in the x-y plane (parallel to the glass plates). The resulting image is a 2D projection of the breast acquired with a controlled sampling rate. Therefore, an improved spatial resolution in the x-y plane (typically 1-2 mm) can be achieved, allowing for smaller morphological and structural information to be resolved.

On the other hand, since the acquired image is a 2D projection of the breast in the x-y plane, it is lacking the depth information in the direction perpendicular to the scan plane. This limitation can be addressed by using diffuse optical tomography (DOT), a different DOI based method, where multiple stationary source-detector pairs are positioned around the breast in either a circular or parallel plate arrangement. By applying inverse reconstruction procedures based on analytical and/or numerical forward “solvers” (they usually solve the diffusion equation), a 3D image of the breast optical properties can be reconstructed [Enfield et al, 2007], [Schmitz et al, 2005] [Choe et al, 2009] [Dehghani et al, 2009]. Although depth information can be achieved through 3D image reconstruction, the problem of low spatial resolution due to the diffusivity of the tissue to NIR light remains in DOT images.

It has been demonstrated [Grosenick et al, 2004] [Kainerstorfer et al, 2013] that depth assessment can be achieved in the 2D scan by using an additional detector that is positioned off-axis from the light source by a certain distance in the x direction. Inhomogeneities captured in the resulting on-axis and off-axis images experience a spatial shift in their location between the two images. The off-axis shift is associated with the depth of the inhomogeneity in the sample space through a theoretical depth-shift curve which is computed based on the solution to the

diffusion equation. Kainerstorfer et al [2013] have characterized the method for different arrangements and orientations of vessel-like structures in phantoms and have measured inhomogeneities depth within 4-7 mm accuracy with respect to the actual depth. The theoretical depth-shift curve has also been used by Grosenick et al [2004] to assess the depths of carcinomas in human breast.

Since the ultimate goal is to use this method to resolve the depth of cancerous areas in the breast, and since there is some inter-patient variation in breast tissue optical properties, the theoretical depth-shift curve has been characterized for different tissue optical properties, inclusion size, breast thickness and the separation between the on-axis and off-axis detectors. It was concluded by Kainerstorfer et al [2013] and Grosenick et al [2004] that the theoretical depth-shift curve for a spherical inclusion in the homogenous slab geometry and for a point-like inclusion in the homogenous infinite medium geometry is only weakly sensitive to variations in the above parameters (for typical values for the breast), possibly making it a universal tool for depth discrimination in the breast.

Preliminary results obtained in our group [Weliwitigoda, 2012] with similar experimental conditions to those reported here showed some discrepancies between the theoretical depth-shift curve and a depth-shift curve that was measured experimentally. These discrepancies required further investigation and were the motivation of this work. Ideally one would want to demonstrate the existence of a universal depth-shift curve which can be derived from diffusion calculations and that can be applied in different geometries and also in practical situations. While breast tissue is a multiplex network of blood and lymphatic vessels, this study utilized an elementary homogenous liquid phantom with a single embedded inclusion in order to simplify the characterization of the experimental depth-shift curve.

Hence, the goals of this study are:

- Characterizing the behavior of the experimental depth-shift curve for variations in the medium optical properties, sample thickness and inclusion size in the homogenous infinite medium geometry.
- Comparing the behavior of the theoretical depth-shift curves with the corresponding experimental curves.
- Defining and explaining the discrepancy between the experimental and theoretical curves.
- Comparing the depths of an inclusion measured by the experimental curve versus the theoretical curve.

## **1.2 Background – Principals of Diffuse Optical Imaging**

### **1.2.1 Light Interaction with Biological Tissue**

Light interacts with matter by exchanging energy quanta known as photons. The two main interactions between light and tissue are absorption and scattering. In absorption, a particle matter transitions from a low energy level to a high energy level with the gap between the levels matching the energy quantum of the incident photon  $h\nu$  (where  $h$  is Plank constant and  $\nu$  the frequency of the radiation). At the macroscopic level, the amount of light that is being absorbed by the medium is quantified by the absorption coefficient,  $\mu_a$  ( $\text{cm}^{-1}$ ), which is defined as the inverse of the mean path a photon traverses in a medium before it is absorbed. Absorption of light by tissue is dependent on the tissue chromophores that absorb the light and on the light wavelength. In the NIR wavelength region (i.e 650-1000 nm), the main tissue absorbers

(chromophores) are oxygenated hemoglobin (HbO<sub>2</sub>), deoxygenated hemoglobin (Hb), water and lipids (Figure 1.1). The absorption of light by each chromophore depends on its concentration in the tissue and on the extinction coefficient as the function of wavelength. Therefore, the total absorption coefficient of a tissue is the summation of the contributions from all the chromophores, and can be written as:

$$\mu_a(\lambda_j) = \sum_{i=1}^M \varepsilon_i(\lambda_j)C_i \quad (1.1)$$

where M is the number of chromophores,  $\varepsilon_i$  ( $M^{-1} \text{ cm}^{-1}$ ) and  $C_i$  (M) are the extinction coefficient and concentration of the  $i^{\text{th}}$  chromophore, respectively, and  $\lambda_j$  is the wavelength (nm).

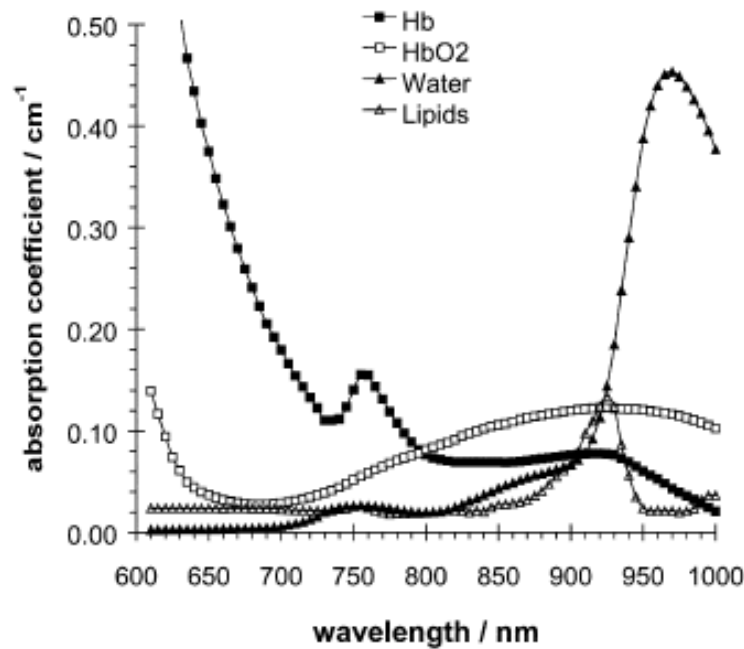


**Figure 1.1** Absorption spectra of Hb, HbO<sub>2</sub>, water and lipids in the near infrared range. The concentrations of Hb and HbO<sub>2</sub> were set to 100  $\mu\text{M}$  [Taroni, 2003]

In biological tissues, while absorption is minimal, scattering is the dominant effect of light interaction in the NIR window. Scattering properties are mainly due to the size of the

structures relative to the incident light wavelength and due to the mismatch in the refractive index between the scattering structures and the medium. Therefore scattering structures in biological tissue are cells and sub-cellular organelles. Since their size is of the order of the incident NIR light and their refractive index is similar to that of the extracellular matrix, they scatter mainly in the forward direction and their scattering properties are weakly dependent on wavelength. The parameter used for describing scattering characteristics at the macroscopic level is the scattering coefficient  $\mu_s$  ( $\text{cm}^{-1}$ ). The scattering coefficient is the inverse of the average distance a photon travels between consecutive scattering events. In diffusion conditions, i.e. when detected photons have experienced many scattering events (usually more than 10) a correct description of light propagation in tissues is obtained by using the reduced scattering coefficient,  $\mu_{s'}$  ( $\text{cm}^{-1}$ ) which is defined as the inverse of the average distance a photon travels before it becomes completely randomized. The average distance a photon travels before a scattering event occurs is called the mean free path (mfp) (Figure 1.2). The inverse of the reduced scattering coefficient is defined as the direct or isotropic mfp (mfp').

The reduced scattering coefficient is related to the scattering coefficient by:  $\mu_{s'} = \mu_s(1-g)$ , where  $g$  is a measure of the anisotropy of the single scattering event. For example, isotropic scattering is characterized by  $g=0$  (however we note that the inverse statement is not true); for  $g=1$  scattering is in the forward direction; for  $g=(-1)$  scattering is in the backward direction. Different degrees of forward or backward scattering are observed when  $g$  is between 0-1 and 0-(-1) respectively (Figure 1.3). In biological tissue,  $g$  is typically 0.75-0.9 [Cheong et al, 1990], thus mainly in the forward direction.

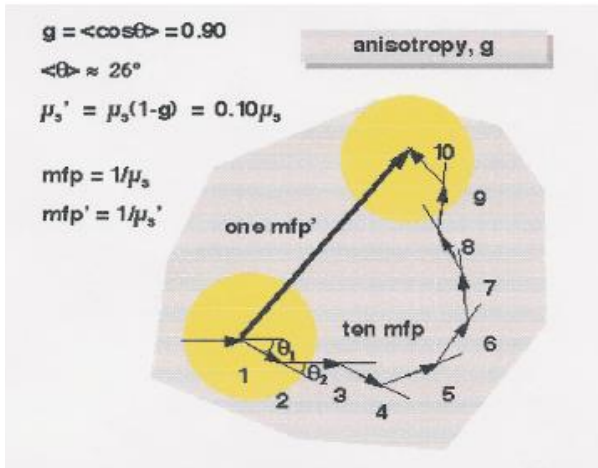


**Figure 1.2** A schematic of how many anisotropic scattering events are equivalent to one isotropic scattering. Each scattering event is dependent on the scattering coefficient  $\mu_s$  and on the scattering angle  $\theta$ . The asymmetry parameter,  $g$ , is given by  $g = \langle \cos \theta \rangle$ . It is used in the expression of the reduced scattering coefficient  $\mu_s' = \mu_s(1-g)$ . [Jacques and Prahl (1998)

<http://omlc.ogi.edu/education/ece532/class3/musp.html>]

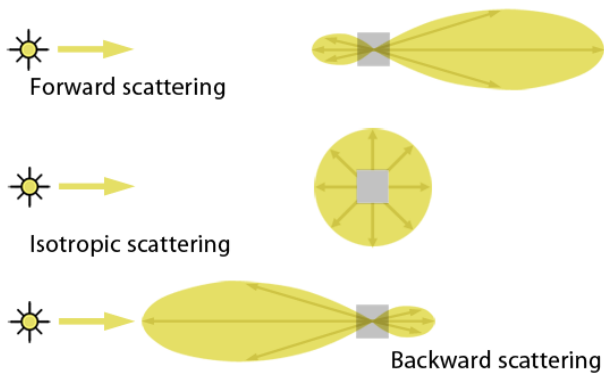


**Figure 1.3:** Forward, backward and isotropic scattering described by using lobes which account for the amount of light being scattered at a given site (represented by the gray square). For isotropic scattering the lobe is a sphere where for forward and backward scattering the front and back lobes are predominant, respectively. [3D Advanced Lessons. <http://www.scratchapixel.com>]

### 1.2.2 Diffuse Optical Imaging

Diffuse optical imaging (DOI) uses near infrared light (NIR) to investigate biological tissues. The 650-1000 nm wavelength range is characterized by a large penetration depth into the tissue, on the order of several centimeters, due to the lower absorption of light by the tissue chromophores at this range. For lower wavelengths light is highly absorbed by hemoglobin and for higher wavelengths by water, making the 650-1000 nm range a medical window for non-invasive diagnostics. At the basis of DOI are the measurements of HbO<sub>2</sub> and Hb absorption spectra and the reconstruction of their concentration in the tissue. Such information can be used for quantitative oximetry, allowing for the assessment of blood oxygenation. Although DOI is characterized by a high intrinsic contrast associated with hemoglobin, the spatial resolution is considered low (6-10mm) [Pogue et al, 2006] due to the diffusive nature of NIR light in the tissue. Figure 1.4 shows a cartoon of the migration of photons from source to detector in a highly scattering medium. The photons are traveling through a volume of the medium (known as the banana shape in reflection mode), with the highest probability at the central darker area. The lighter shades represent regions of tissue reached by photons that travel along longer paths on their way from source to detector, thereby negatively affecting the spatial resolution. The problem of low spatial resolution can be partly addressed by using two-dimensional (2D) planar scanning, where the spatial sampling can be controlled [Grosenick et al, 2004], [Yu et al, 2010], [Weliwitigoda, 2012], [Kainerstorfer et al, 2013].

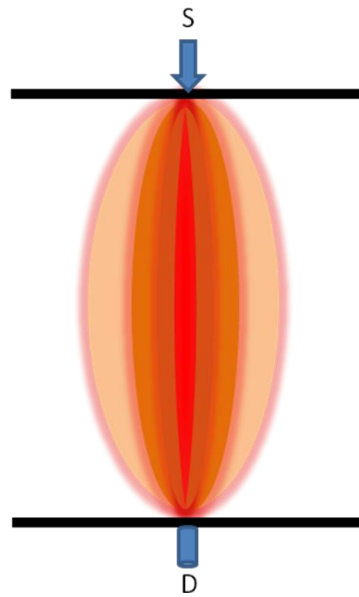


**Figure 1.4** Sensitivity map of photons migrating from source (*S*) to detector (*D*) and passing through a diffusive medium (i.e breast tissue) in transmission mode. Darker shades in the central area signify a higher probability for the detected photons to pass through those regions.

There are two main configurations for source-detector coupling in DOI – reflection and transmission. In transmission mode the source and detector are positioned on opposite sides of the sample and the detected photons are those which traverse through the tissue and get collected on the other side. In this configuration the light energy density inside the medium is usually described by the solution for the diffusion equation in the slab geometry. In reflection mode the source and detector are positioned on the same side of the sample, at some distance from each other (typically 1-3 cm) [Fantini et al, 1999], and the collected photons are the ones being reflected backwards after penetrating the tissue. This configuration is utilized when the sample is too thick for the photons to be transmitted and detected on the other side, such as in brain measurements.

### 1.2.3 Optical Mammography System

One of the applications for DOI is optical imaging of the breast for the detection, diagnosis and treatment monitoring of breast cancer. There are three main types of optical mammography methods – continuous wave domain (CW), frequency domain (FD) and time domain (TD).

In continuous wave domain systems the source of light is a steady-state source, either a laser (with discrete emission wavelengths) or a lamp with a broadband spectrum in the NIR region, thus providing rich spectral information. CW systems are characterized by a high signal-to-noise ratio (SNR), easy implementation and lower cost compared to the other two systems. A drawback of CW systems is the difficulty to separate absorption from scattering properties of tissues.

In frequency domain (FD) systems one transmits discrete wavelengths of modulated light in the NIR region and it is possible to measure the DC (average intensity), AC (amplitude) and phase information of the transmitted signal through the tissue. Modulation of the emitted light enables one to quantify not only the attenuation of light intensity with source-detector separation but also the average time delay between the emitted and collected photons; the knowledge of these two parameters allows for the separation of absorption from scattering properties of tissue. For this purpose, the light source needs to be modulated at radio frequencies, typically between 25 MHz and 1 GHz [Jacques and Pogue, 2008]. Typical wavelengths used in FD systems are 690 and 830 nm [Fantini, 1998] where one can take advantage of the difference in the absorption spectra between HbO<sub>2</sub> and Hb.

Time domain (TD) systems are the most complicated and expensive of all three. These systems measure the temporal point spread function (TPSF) of the detected photons. With time

domain methods it is also possible to resolve scattering from absorption properties of tissues [Grosenick, 2003]. The source of light, typically an ultra-short pulsed laser ( $\sim$  picoseconds) with a high repetition rate ( $\sim$  100 MHz), emits very short pulses of photons into the medium which then take a finite amount of time to reach the detector. The temporal spread of detected photons which is the impulse response of the system in the time domain can be modeled by using the solution of the diffusion equation for a Dirac  $\delta$  pulse in order to retrieve both absorption and reduced scattering coefficient. The TPSF can also be divided into time windows, each carrying different information about the regions of tissue probed by the photons. For example, earlier time windows account for photons that travel in more linear trajectories between source and detector, therefore experiencing less scattering events. The information from the different time windows can be used to perform spatial reconstruction of the sample optical properties. TD systems require sensitive and efficient detection systems to be able to collect the photons that are emitted with the high repetition frequencies, resulting in costly and harder to implement systems in comparison with the CW and FD systems.

#### **1.2.4 The Diffusion Equation**

The migration of photons in biological tissue can be modeled by the radiative transfer equation (RTE or the Boltzman equation) which describes the energy balance in a volume element in a unit solid angle per unit time. Since biological tissue is a highly scattering medium, certain assumptions can be made that simplify the RTE into the Diffusion Equation.

The assumptions made are:

1. The number of scattering events is much larger than absorption events ( $\mu_s \gg \mu_a$ ) i.e. light becomes isotropic after few scattering events (usually around 10 for typical tissues optical properties).
2. Time variations in the optical energy density and in the source occur in a time scale much longer than the average time between one collision to another (the time it takes for one mfp).
3. The source is isotropic.

As will be described in the following sections the work in this study was performed with a CW domain system.

In the CW domain the diffusion equation is given by:

$$-D\nabla^2\phi_o(\vec{r}) + \mu_a\phi_o(\vec{r}) = \delta(\vec{r}) \quad (1.2)$$

where  $\phi_o$  is the fluence [ $\text{cm}^{-2}$ ] or the attenuation of light per unit surface,  $D$  is the diffusion coefficient given by  $1/(3\mu_s + \mu_a)$ ,  $\mu_a$  and  $\mu_s$  are the absorption and reduced scattering coefficients respectively [ $\text{cm}^{-1}$ ],  $\delta(\vec{r})$  is the Dirac delta function and  $\vec{r}$  is the observation point.

In Eq.(1.2) we have considered the case of homogeneous medium, i.e. the absorption and reduced scattering coefficient are constant, but in a general situation they also may vary inside the medium (heterogeneous medium).

The solution to the standard diffusion equation depends on the geometry of the medium and on the appropriate boundary conditions. Typical geometries where analytical solutions to the diffusion equation can be derived are the regularly bounded geometries like infinite (no

boundary), semi-infinite and slab. The infinite geometry is the ideal case where no boundary conditions need to be applied as the source and detector are both immersed inside the medium and the medium is considered to be infinite in all directions. In the semi-infinite geometry one side of the medium interfaces with the source and detector, hence boundary conditions need to be applied for that side. In the slab geometry, the source and detector interface with the medium on opposite sides requiring boundary conditions to be applied on both sides.

The work in this study was done in the infinite medium geometry as our aim was to first test the experimental depth-shift curve under the ideal conditions.

Since the right hand-side of Equation (1.2) is a  $\delta$  Dirac function, the solution to  $\phi_o$  in the infinite medium geometry is given by the Green's function:

$$g(\vec{r}) = \phi_o(\vec{r}) = \frac{1}{4\pi D} \frac{e^{-\mu_{eff} \vec{r}}}{\vec{r}} \quad (1.3)$$

where  $\mu_{eff} = \sqrt{3\mu_a\mu_s}$ .

For the simplified case of an infinite homogenous diffusive medium with an embedded absorbing inhomogeneity, the diffusion equation is solved by using Perturbation Theory.

An inclusion having contrast  $\Delta\mu_a$  is introduced into the medium such that the fluence is now given by:

$$\phi_o + \Delta\phi = \phi \quad (1.4)$$

The equation for  $\Delta\phi$  can be obtained after some calculations and after neglecting higher order terms:

$$-D\nabla^2(\Delta\phi) + \mu_a\Delta\phi = -\Delta\mu_a\phi_o \quad (1.5)$$

Equation (1.5) is similar to equation (1.2) except that the  $\delta$  Dirac source term is replaced by a new source term on the right hand side of Equation (1.5) and  $\phi_o$  is replaced by  $\Delta\phi$ . For linear

systems, the output of the system (in our case  $\Delta\phi$ ) is given by the convolution of the new source term with the system response (Green's function). Therefore:

$$\Delta\phi = \phi - \phi_o = -\Delta\mu_a\phi_o \otimes g(r) \quad (1.6)$$

Assuming the linear size of the inclusion,  $d$ , is  $d \ll |\vec{r}'|$  and  $|\vec{r} - \vec{r}'|$  ( $\vec{r}'$  is the position vector of the inclusion, Figure 1.5) and that  $\Delta\mu_a$  is constant inside the inclusion, the solution for  $\Delta\phi$  is:

$$\Delta\phi(|\vec{r}|) \approx -\Delta\mu_a V \phi_o(|\vec{r}'|) \phi_o(|\vec{r} - \vec{r}'|) \quad (1.7)$$

where  $V$  is the volume of the inclusion. Equation (1.7) describes the change of fluence at the presence of a perturbation centered in  $\vec{r}'$  when the detector is in  $\vec{r}$ . The use of the above solution is explained in the following section.

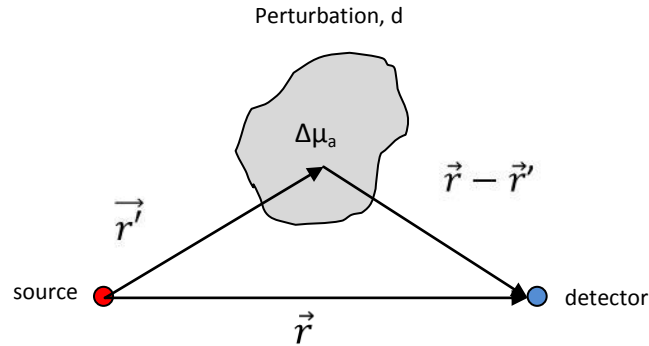


**Figure 1.5** Perturbation with linear size  $d$  and absorption coefficient  $\Delta\mu_a$  is positioned at  $\vec{r}'$  from the source. The detector is positioned at  $\vec{r} - \vec{r}'$  from the perturbation. Assuming  $d \ll |\vec{r}'|$ ,  $d \ll |\vec{r} - \vec{r}'|$  and  $\Delta\mu_a$  constant, the change of fluence at the presence of a perturbation can be described by Equation (1.7).

### 1.2.5 Depth Discrimination in 2D Planar Scanning

In 2D planar-scanning, the breast is slightly compressed between two parallel glass plates and a collinear source-detector pair, located behind the top and bottom glasses, performs the scan in the x-y plane (Figure 1.6). The image acquired is a 2D optical intensity projection of the scanned area, where lower intensity values represent absorbing features. The increased spatial resolution is achieved by a controlled spatial sampling rate in the x-y plane (typically, one acquisition every 1-2 mm is an adequate choice). However it should be noted that because of the particular way photon migration occurs (see the photon sensitivity map Figure 1.4) the structures that benefit more from a higher spatial sampling are those located close to source or detector whereas the effect on deeper structures is more moderate.

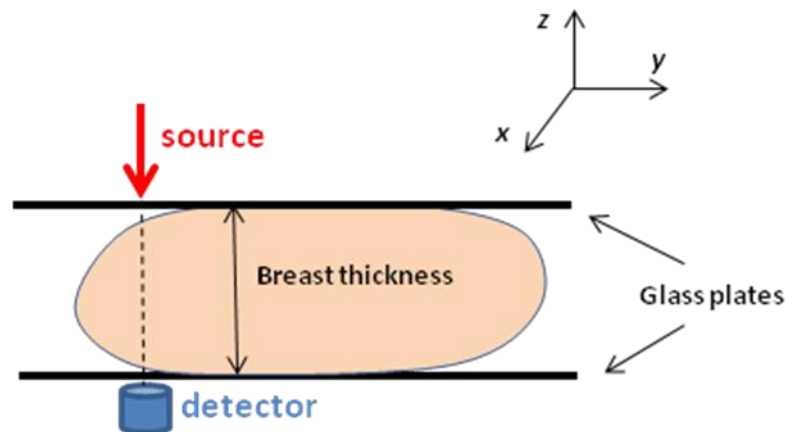


**Figure 1.6** A typical setup of a 2D planar-scanner utilized in optical mammography. The breast is slightly compressed between two glass plates. A collinear source-detector pair scans the breast in the x-y plane, and the resulting image is a 2D projection of the breast. In this configuration no information is acquired in the depth direction (z-axis).

Since the resulting images are 2D projections of the breast they lack any information in the depth direction (z-axis). Adding depth information to a 2D planar-scanning of the breast was

first reported by Grosenick et al [2004] in time domain. To obtain the depth information, a second detector was added such that one detector was on-axis ( $D_{ON}$ ) with the source fiber (S) and the second detector was positioned off-axis from the source ( $D_{OFF}$ ) and in a distance  $\delta D$  from  $D_{ON}$  (Figure 1.7) ( $\delta D$  is referred to as inter-detector separation or D-D).

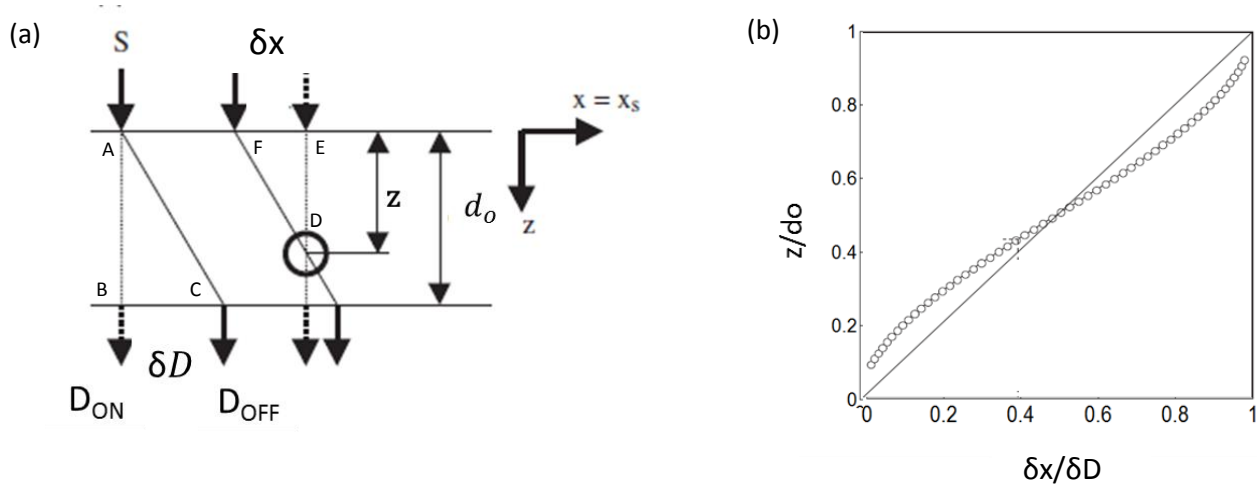


**Figure 1.7** (a) A simplified depiction of a single inhomogeneity (open circle) embedded in a medium and scanned with a configuration of a source and two detectors in the x-y plane.  $Z$  is the inhomogeneity's depth and  $d_o$  is the distance between the source and detectors plane (S-D separation).  $D_{ON}$  is on-axis with the source whereas  $D_{OFF}$  is off-axis by some distance  $\delta D$ . The spatial location of the detected inhomogeneity is therefore shifted by  $\delta x$  between the on-axis and off-axis images. The diagonal line in (b) is the relation  $z/d_o = \delta x/\delta D$ . The open-circles curve represents the relative shifts according to diffusion theory. [modified from Grosenick et al, 2004]

In Fig. (1.7) the depth of the inhomogeneity is represented by  $z$ , and  $d_o$  is the distance between the source and detectors plane (S-D separation), also defined as the sample thickness in the slab geometry medium. When performing a line scan of such a medium in the x direction, the optical intensity curve experiences a negative peak (minimum) due to the absorption of light by the inhomogeneity (Figure 1.8-a). The same minimum is present in the intensity curve of the off-axis

detector, but it is shifted by a distance  $\delta x$  from the minimum detected by  $D_{ON}$  (Figure 1.8-b) and which depends on the depth location of the inclusion.

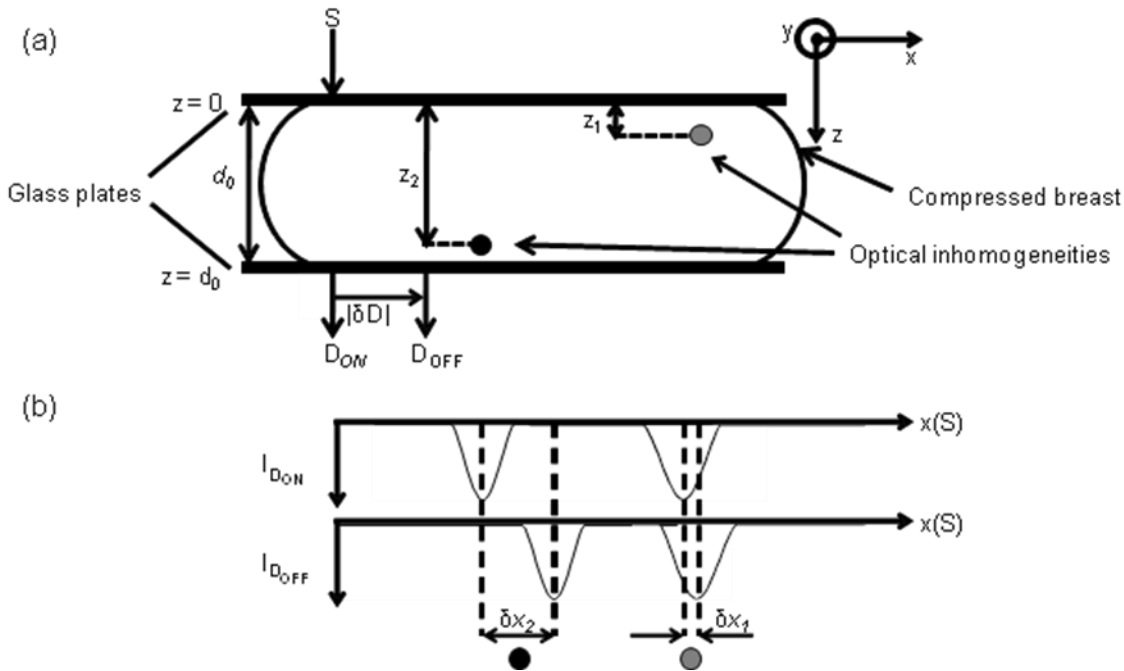


**Figure 1.8** (a) Two absorbing inhomogeneities are embedded in the sample in deeper ( $z_2$ , black circle) and shallower ( $z_1$ , gray circle) depths with respect to the source. (b) The negative intensity peaks that result from the absorption of light by the inhomogeneities are shifted by some distance  $\delta x$  between the on-axis and off-axis images. The deeper the inclusion within the sample, the greater is the value of  $\delta x$ . [modified from Kainerstorfer et al, 2013]

By using the similarity between the triangles ABC and DEF of Fig. 1.7 we can easily derive the relationship  $z/d_0 = \delta x / \delta D$ , which is the diagonal line in Figure 1.7-b and which relates the shift  $\delta x$  between the two minima to the depth of the inhomogeneity. However, the diagonal line is not the true representation of photon migration from source to detector; thus, the depth ( $z$ ) of the inclusion cannot be simply extracted from the above relation. For describing photon migration from source to detector in a diffusive medium containing an absorbing perturbation, Grosenick et

al used a solution to the diffusion equation for an absorbing sphere (radius = 0.5 cm,  $\mu_s = 10 \text{ cm}^{-1}$ ,  $\mu_a = 0.16 \text{ cm}^{-1}$ ) in a homogenous slab ( $d_o = 6.5 \text{ cm}$ ,  $\mu_s = 10 \text{ cm}^{-1}$ ,  $\mu_a = 0.04 \text{ cm}^{-1}$ ). The solution was found for different depths of the sphere within the medium, and those depths were related to the corresponding off-axis shifts ( $\delta x$ ) in order to create the depth-shift curve (open circles in Figure 1.7). The value of  $\delta x$  varies as a function of the inclusion depth – the deeper the inclusion the larger  $\delta x$ . The shape of the depth-shift curve is determined by the shape of the light bundle which is the visitation area for photons migrating from source to detector in the medium (Figure 1.4).

The theoretical depth-shift curve can be used to extract the unknown depth of an inclusion embedded in a medium: assuming that  $d_o$  and  $\delta D$  are known and  $\delta x$  is measured from the difference in the location of the minima between the two images, the depth  $z$  can be extracted from the depth-shift curve. According to Grosenick et al [2004] and Kainerstorfer et al [2013], the depth-shift curve is insensitive to the inclusion radius,  $\delta D$ ,  $d_o$  and the background optical properties (for typical breast values of 4-7 cm in breast thickness and  $0.03\text{-}0.15 \text{ cm}^{-1}$  in background absorption coefficient [Tromberg et al, 1997], [Shah et al, 2001], [Durduran et al, 2002] ). These observations were reported for a spherical inclusion in a homogenous slab geometry [Grosenick et al, 2004] and point-like inclusion in infinite medium geometry [Kainerstorfer et al, 2013].

The depth discrimination method described above is relatively simple to implement, however a few points should be noted as to the accuracy of the method. The theoretical curve is based on the solution to the diffusion equation which assumes an isotropic source and isotropic scattering. Since the reduced scattering coefficient of the medium is on the order of  $1 \text{ mm}^{-1}$ , the isotropic mean free path (mfp') of the photons is  $\sim 1 \text{ mm}$ . On the contrary, biological tissues have

anisotropy of 0.7-0.9, thus the scattering coefficient is  $\sim 10 \text{ mm}^{-1}$  and the photons mfp is only  $\sim 0.1 \text{ mm}$  (ten times shorter than in the theoretical model). In real tissue, for an inclusion closer to the source there are in fact many more scattering events before a photon hits the inclusion compared to the theoretical model. Also, in reality the source is not isotropic, thus close to the source the photons still carry the memory of their initial directionality. As a result, we might expect some errors when the theoretical curve is used for retrieving the depth of an inclusion which is located close to the source. Deeper into the tissue the photons become completely randomized, thus minimizing the discrepancy between the theoretical model and the reality. The theoretical curve becomes approximate also close to the boundaries since the diffusion equation cannot exactly incorporate the phenomenon of reflection at the boundaries.

In light of the above mentioned limitations of the theoretical curve, and since our preliminary work [Weliwitigoda, 2012] demonstrated a discrepancy between the theoretical depth-shift curve and an experimental depth-shift curve that was measured for the same variables as in the theoretical model, we were interested in obtaining an experimental confirmation for the behavior of the theoretical depth-shift curve under realistic conditions that may not meet the ideal situation of the model. As a first step we decided to investigate the sensitivity of the curve to breast tissue variables by using the simplest geometry of a homogenous infinite medium with a single absorbing cylindrical inclusion, where no boundary conditions are considered. The rationale for choosing this geometry was also based on a preliminary comparison between theoretical curves for slab versus infinite geometries which showed a negligible discrepancy of 1.5 mm in depth. Assuming that the theoretical curve cannot be reproduced under realistic conditions, another aim was determining whether such a discrepancy requires the derivation of various experimental curves for different optical mammography instruments.

The following chapter describes the methods used to construct the experimental depth-shift curve.

## **Chapter II - Methods**

### **2.1 Instrumentation for Measuring the Experimental Depth-Shift Curve**

The schematic of the experimental setup is provided in Figure 2.1. The main components of the setup included a commercial Oximeter (OxiplexTS, ISS Inc., Champaign, IL) that emitted and detected NIR light, a computer to program and control the oximeter (BOxy software, ISS Inc), a liquid phantom with embedded source and detector fibers in an infinite geometry configuration, a microstepper scanner (isel-automation, Germany) to move the source-detectors arrangement, a computer to program and control the microstepper (Techno-isel, New Hyde Park, NY) and a computer with Matlab software (MathWorks, Inc) for data processing. A detailed description of the system is provided in the following sections.

The oximeter included 8 laser diode sources of 690 nm wavelength, another 8 sources of 830 nm wavelength and two photomultiplier tubes (PMT A and PMT B). Modulation of the emitted light at 110 MHz was achieved by activating an external switch. To down convert the modulation frequency an optical heterodyne technique was applied by modulating the PMTs gain to 110.005 MHz and low passing the signal to the cross-correlation frequency of 5 KHz. The signal was then digitized by an A/D converter and underwent a Fast Fourier Transform to calculate the DC, AC and phase components of the signal. Although only one laser diode was used in the described experiments, the oximeter had also a multiplexing capability for the simultaneous activation and detection of laser sources with the same wavelength.

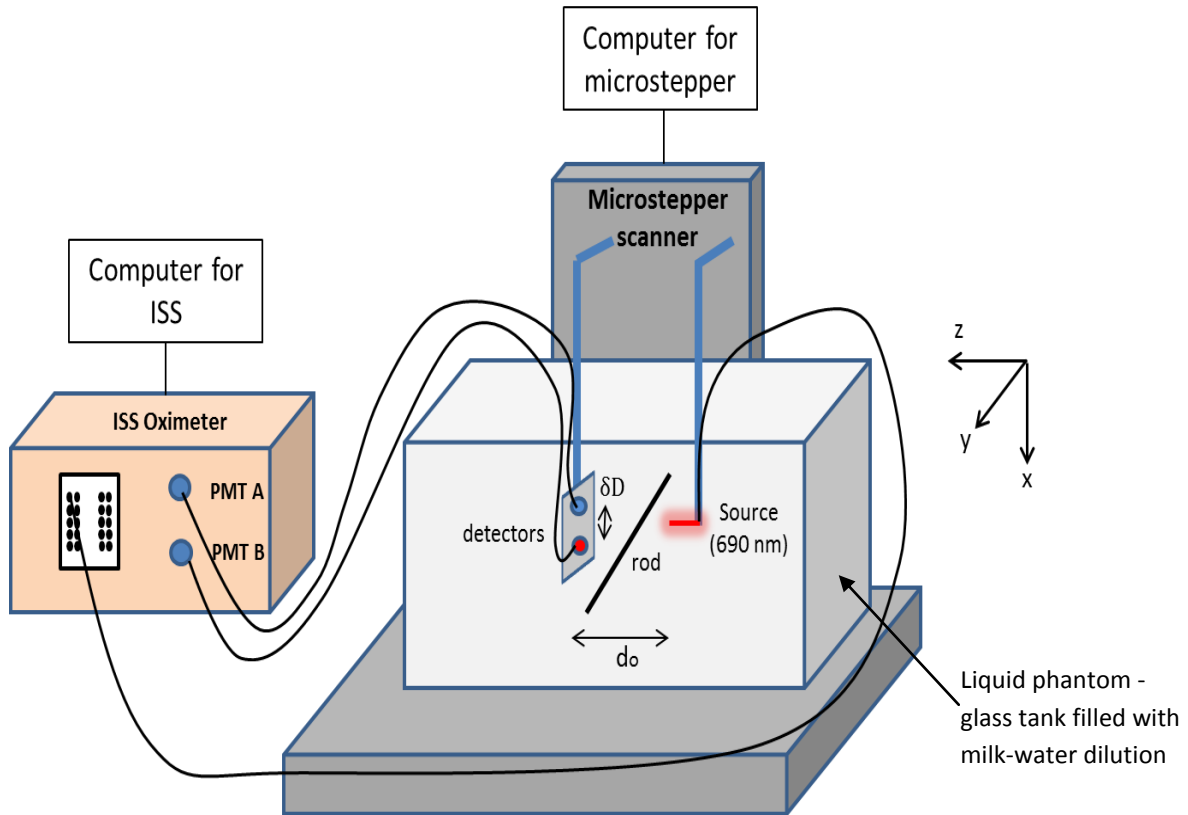


**Figure 2.1** A schematic representation of the experimental system that was used to measure the experimental depth-shift curves. The main parts of the set up are a liquid phantom made of a glass tank filled with milk-water dilution; source fiber and two off-axis detectors submerged in the medium on one end and connected to an ISS oximeter on the other end; a single black rod as the absorbing inhomogeneity; a microstepper scanner to scan the source-detectors array. The rod was kept stationary and the source-detectors pairs were scanned along  $x$  from top to bottom, afterwards advancing in 1 mm in the  $-z$  direction and repeating the scan along  $x$  etc. Acquisition was carried out in the  $+x$  direction only.

For the experiments whose purpose was measuring the experimental depth-shift curve one 690 nm laser source and both PMTs were used. An 800  $\mu\text{m}$  diameter optical source fiber was connected to the oximeter on one end and to a holder on the other hand. The holder included a slit which enabled adjusting the distance of the source fiber with relation to the detectors by

sliding it forward/backward (Figure 2.2). The holder was positioned on a post which was connected to the microstepper motor.

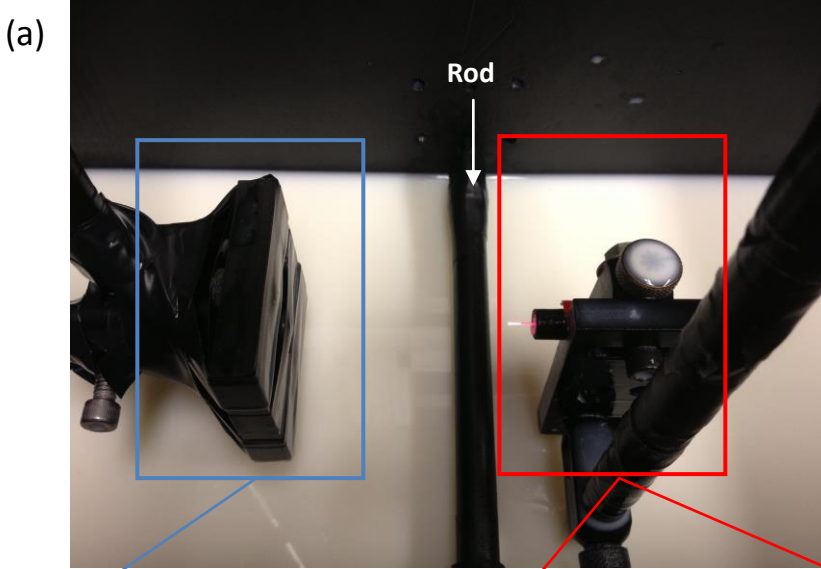
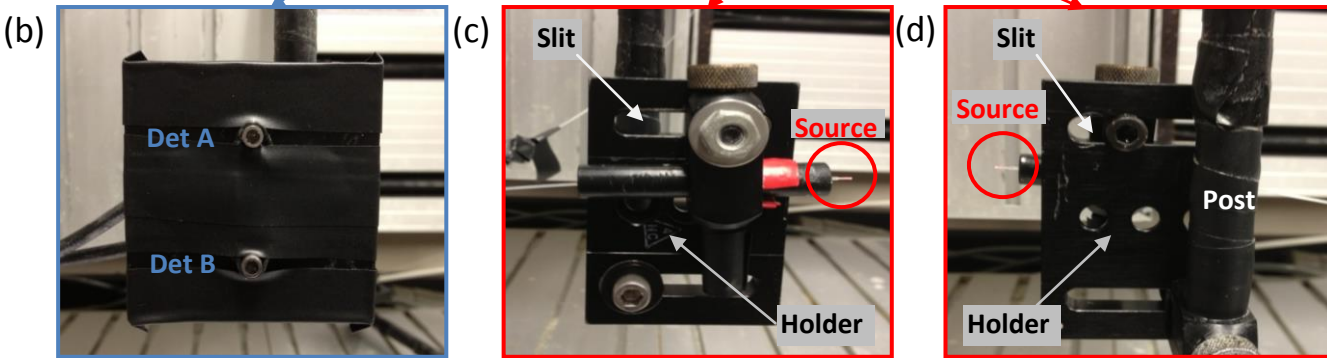


**Figure 2.2** (a) The source (red frame) mounted on a holder and facing the two off-axis detectors (blue frame) that are mounted on a second holder. A black Delrin rod is fixed horizontally on the tank's walls in the space between the source-detectors configuration. During an actual scan the milk-water dilution covers the entire configuration. Figures (b-d) show a close-up angle of the holders with the source and detectors.



Two 5 mm diameter detector fibers were connected to PMTs A and B in the oximeter on one end and to a holder on the other end. The holder included a slit in which the detector fibers were placed and which enabled sliding the fibers to adjust the separation distance between them. The source fiber holder and the detectors holder were positioned on two separate posts that were connected to the microstepper. The source fiber tip was aligned to be in a straight line to the

middle point between the two detectors, and perpendicular to the detectors plane, such that both detectors were off-axis with respect to the source with equal distances  $\delta D/2$  (Figure 2.3).

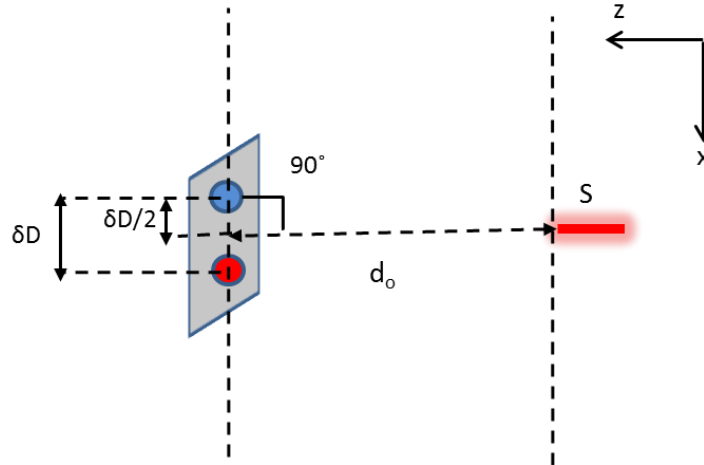


**Figure 2.3** The source's tip (S) was position perpendicular to the detectors plane, facing the midpoint between the two detectors and with a distance  $d_o$ .

The source and detectors were submerged in a liquid phantom which was set up as the following: a glass tank with dimensions  $20 \times 25 \times 40 \text{ cm}^3$  was filled with 18 liters of a milk-water dilution that had a volumetric ratio of 3:5 (2% reduced fat milk and tap water). The optical properties of the liquid were measured as will be described later and were determined to be  $\mu_s \approx 8 \text{ cm}^{-1}$  and  $\mu_a \approx 0.005 \text{ cm}^{-1}$  at a wavelength of 690 nm. This specific dilution was chosen as it had a scattering coefficient similar to that of breast tissue. The clear glass sides and bottom of the tank were covered with black PVC panels that were placed on the inside of the tank. The purpose of using the panels was to absorb any photons that might propagate to the borders and prevent them from backscattering into the detectors. For the same reason, the posts holding the source and detectors were covered with black tape. The dimensions of the tank were large enough to simulate infinite geometry [Weliwitigoda, 2012]. A single black Delrin rod, 20 cm in length was used as the

absorbing inhomogeneity and was fixed on both ends with the help of grooves in the side black panels. For most of the experiments a 3.5 mm diameter rod was used with an exception of the experiment where the inclusion size was varied in order to test its effect on the depth-shift curve.

## **2.2 Data Acquisition**

The movement of the source-detectors (S-D) arrangement was controlled by the microstepper motors. A trigger signal, output by the microstepper was sent to the oximeter and synchronized the sampling of data with the motors movement. The black rod was positioned horizontally, in the middle of the tank, such that its length was parallel to the tank's floor. It was kept stationary while the S-D arrangement was scanned along the +x direction for about 70 mm and afterwards advancing 1 mm in the -z direction (Figure 2.4). The scan along +x was repeated etc. In the z direction, the scan started with the source fiber tip positioned 1 mm away from the rod's surface and ended with the surface of the rod located 1-3 mm away from the detectors plane. Each scan line in the +x direction started with the fiber tip positioned about 35 mm above the surface of the rod and ended 35 mm below the surface of the rod. Previous experiments [Weliwitigoda, 2012] demonstrated that acquiring data in both +x and -x directions causes a shift between pixels in even versus odd numbered rows, therefore, data were acquired in the +x direction only.

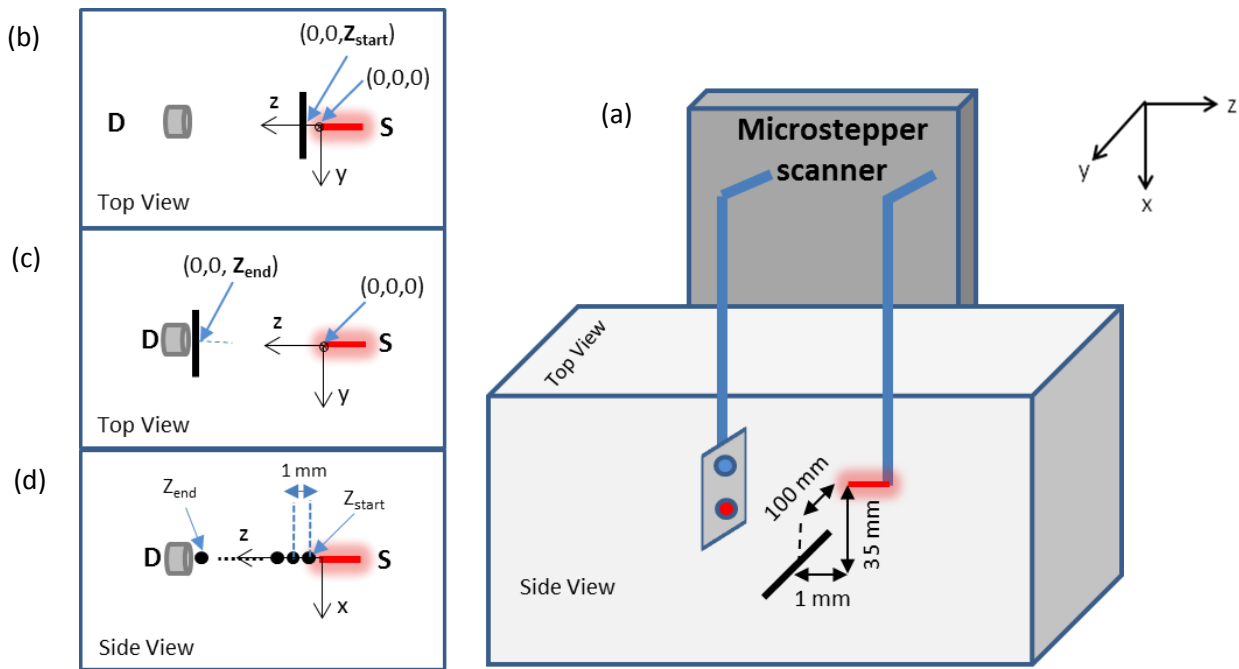


**Figure 2.4** (a) A 3D view of the starting position of the scan. The fiber tip is positioned 35 mm above and 1 mm away from the surface of the rod. (b-c) Top views of the S-D configuration at the beginning of the scan (b) and at the end of the scan (c). (d) Side view of the S-D configuration from the start position where the rod is close to the source until the end position close to the detectors.

The oximeter was triggered by the microstepper to start acquiring at the beginning of each line and it was programmed to stop after 36 points (corresponding to 70 mm). It was set to wait for the next trigger which was given when the source-detectors configuration was back to its position at 35 mm above the rod. A sampling rate of  $0.5 \text{ mm}^{-1}$  was achieved by setting the motor speed to 10mm/sec and the sampling frequency of the ISS oximeter to 5 Hz. Therefore, each scan line of 70 mm included 36 points with a  $2 \times 1 \text{ mm}^2$  pixel size. The reference system was fixed with its origin at the tip of the source fiber and the axis oriented as in Fig.2.4 .

**Note:** The described instrumentation and data acquisition method were existing methods that had already been used in similar depth discrimination experiments [Weliwitigoda, 2012]. Calibration

issues and noise characterization were discussed in detail and it was determined that the image space being scanned within the liquid phantom should be considered an infinite medium geometry based on the findings that the boundaries of the image are not affected by their proximity to the PVC covered tank's walls.

## **2.3 Raw Data Processing**

Data analysis was performed by using Matlab. In order to measure the depth-shift curve, the following main steps were executed: (1) spatial processing, (2) intensity minima identification, (3) generating the plot of depth-shift curve.

### **2.3.1 Spatial Processing**

The raw data included intensity values along each scan line with an intensity minimum at the location of the rod. In the spatial processing step the raw data from detectors A and B were spatially mapped into 2D matrices of 36 rows and a certain number of columns, depending on how many depths were acquired (or how many lines were scanned). For example, for a  $d_0$  of 65 mm, typically 58 lines were scanned, thus the number of columns would be 58 (Figure 2.5).

Following the reshaping of raw data into a 2D matrix, the data points along each line were interpolated from 2 mm to a 0.5 mm pixel size, increasing the sampling rate from  $0.5 \text{ mm}^{-1}$  to  $2.0 \text{ mm}^{-1}$ . The number of rows in the 2D matrix therefore increased from 36 to 144. This resulted in smoother data lines, enabling a more accurate identification of the negative peaks and a depth-shift curve with a higher resolution.

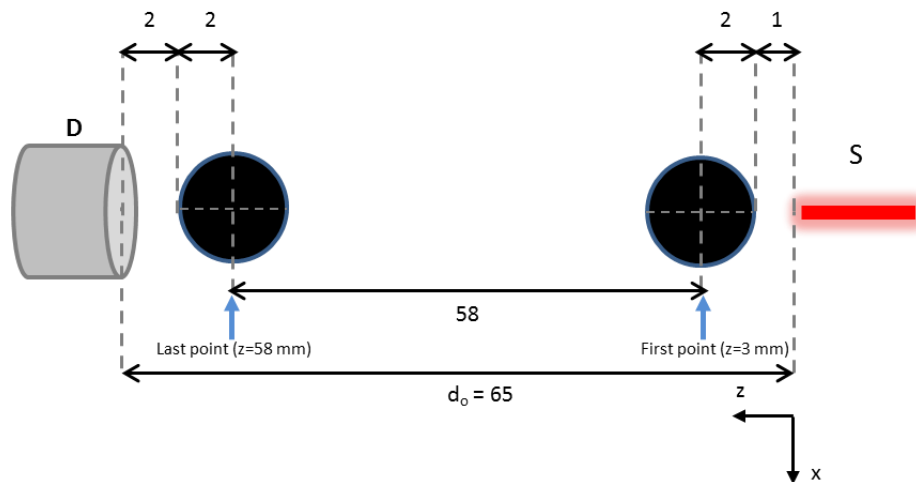


**Figure 2.5** A schematic showing a side view of the S-D configuration and the rod at its start and end points for a specific S-D separation ( $d_0$ ) of 65 mm. The first point was measured from the tip of the source to the center of the rod while the last point was determined when the rod's surface was typically located 2 mm away from the detectors plane.

### 2.3.2 Intensity Minima Identification

The minimum intensity value in each scan line was identified by using the “min” function in Matlab. Since the setup included a single absorbing rod in a highly scattering medium, the intensity curve had a distinct negative peak at the location of the rod and there was no need to apply additional algorithms (i. second derivative) in order to identify the minimum point (Figure 2.6). In most cases a single pixel could be identified as having the minimum value. In the cases where two neighboring pixels had similar minimum intensity values, these pixel numbers were averaged and the mean pixel number was considered as having the minimum intensity.

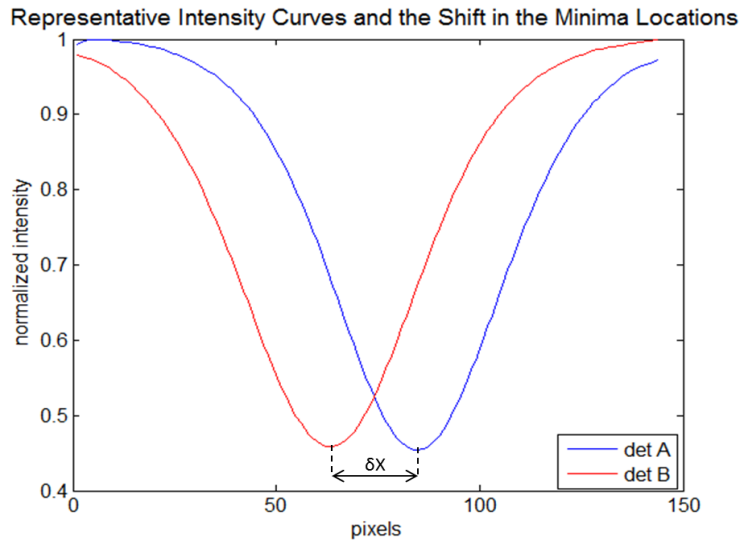


**Figure 2.6** Normalized optical intensity curves (raw data) showing the negative peaks that result from the absorption of light by the black rod. The pixels which carry the minimum intensity values are identified and the spatial distance between them is defined as  $\delta X$ .

The pixels that were identified as carrying the minima values were formed into two arrays (namely A and B), one for each detector. Since arrays A and B contained discrete pixel values whose size was limited by the spatial resolution, some  $\delta x$  values were associated with a range of  $z$  values. This issue is demonstrated in Figure 2.7 where the pixels that were identified as carrying the minimum intensity at each depth (for detector A only) are plotted versus the actual depths of the inclusion in the S-D space (blue line). Connecting the discrete pixel numbers into a continuous line resulted in a steps-like graph such that some shift values did not have a corresponding unique depth but rather a range of possible values. This issue carried on to the final depth-shift curve, increasing the error between actual and measured depths that were obtained by using this curve.

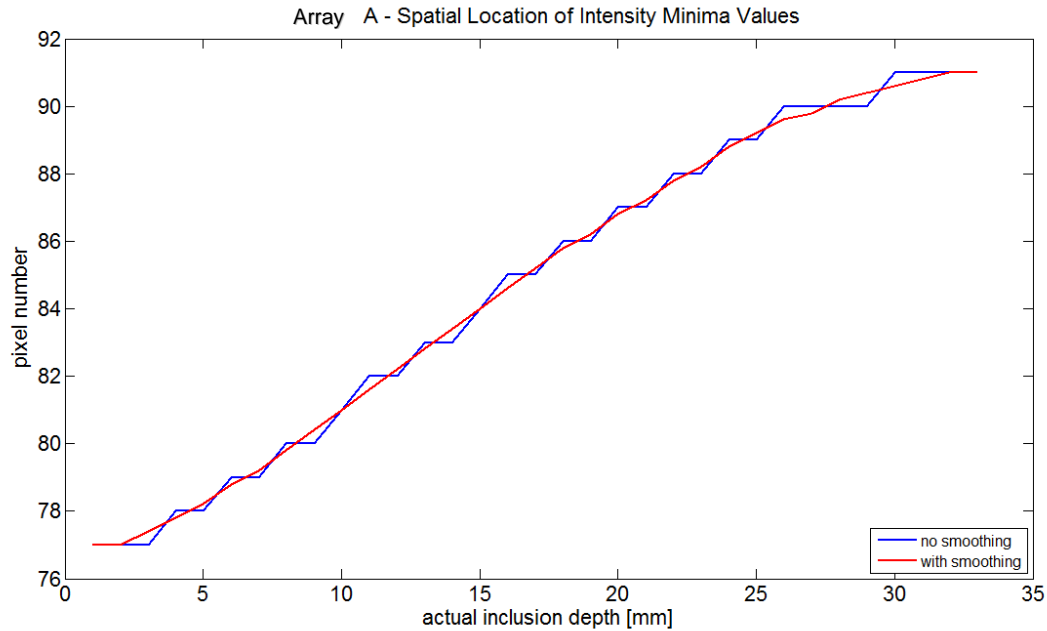


**Figure 2.7** A plot of a representative array A of the pixel numbers that were identified as having minimum intensity values at each depth of the inclusion in the S-D space. The blue curve was plotted by connecting the discrete pixel values. Due to the limited spatial resolution, some of the shift values are associated with a range of depths, increasing the error of the calculated depth. Smoothing the discrete values into a continuous curve (red line) improved the depth resolution and decreased the error.

To address this issue we smoothed each of the arrays A and B into continuous curves and thus averaged the pixel values between each neighboring pair of discrete pixels. The smoothed curve is presented in red in Figure 2.7. The resulting depth-shift curve had a finer depth resolution, enabling a more precise depth measurement of the inclusion.

### 2.3.3 Generating the Depth-Shift Curve

In the final step of the raw data processing the depth curve was generated by using the off-axis shift information that was obtained in the previous step (section 2.3.2). Two new arrays were defined:

1.  $\delta x / \delta D$  – the shifts between off-axis minima multiplied by the pixel size (0.5 mm) and normalized by the inter-detector separation (D-D)
2.  $z/d_0$  – the distance between the source fiber tip and the detectors' plane (S-D or  $d_0$ ) was measured by a ruler. The  $z$  values are the distances between the source tip and the center of the rod.

To generate the final depth-shift curve, the vector  $z/d_0$  was plotted versus vector  $\delta x / \delta D$  (Figure 2.8).

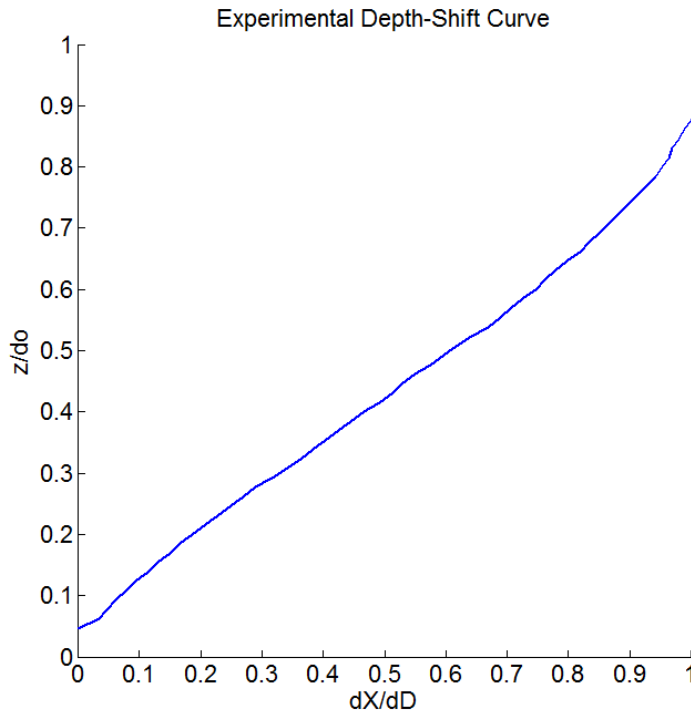


**Figure 2.8** A plot of the experimental depth-shift curve for the experimental conditions of S-D 65 mm, D-D 19.3 mm,  $\mu_a$  0.005  $\text{cm}^{-1}$ ,  $D_{rod}$  3.5 mm.

## **2.4 Determining Depth-Shift Curves Based on Diffusion Theory**

Since we were interested in investigating the behavior of the experimental depth-shift curve for the same variables as in the theoretical model, we used corresponding theoretical depth-shift curves as references. The theoretical curves were computed in Matlab by using the numerical solution to the diffusion equation, specifically the first-order perturbation theory (Born Approximation). The calculations assumed an effective point source that was placed at a distance  $1/\mu_s$  from the source's tip. The curves were computed by using the same variables ( $\mu_a$ ,  $\mu_s$ , S-D separation, D-D separation,  $D_{rod}$ , inclusion geometry and medium geometry) that were used experimentally with the exception of using point-like source and detectors. The depth of the inclusion,  $z$ , was defined from the source fiber tip to the center of the inclusion. It should be noted that the physical setup of using posts and holders to position the source-detectors configuration inside the medium was not accounted for in the theoretical computations. The comparison between the experimental and theoretical depth-shift curves is presented in the Results section.

## **Chapter III – Experimental Protocols**

### **3.1 Absolute Measurements of Background Optical Properties**

The optical properties of the medium were one of the variables we were interested in with regards to their effect on the depth-shift curve. In order to change this variable experimentally we added diluted India ink to the milk-water medium to increase the absorption coefficient to typical values found in the breast ( $0.03-0.15 \text{ cm}^{-1}$ ). Before conducting the actual experiment of

measuring the depth-shift curve at different absorptions we performed measurements of the optical properties of the medium in order to obtain the absolute values of the absorption and reduced scattering coefficients for different concentrations of ink. This section goes into the details of how we performed these measurements.

### 3.1.1 Formulation of diluted India ink

A concentrated Higgins India ink was diluted with de-ionized (DI) water according to a recipe provided by [Martelli and Zaccanti, 2007]. The recipe enabled rapid calculations of the quantities of intralipid, water and ink that are necessary to achieve a liquid phantom with the desired optical properties. In our experiments we used milk instead of the intralipid as its optical characteristics are similar to the intralipid and it could be more readily obtained.

The pure ink was first diluted to a concentration of  $\rho_{\text{dilution}} = 0.007369$  according to Equation 3.1:

$$\rho_{\text{dilution}} = \frac{W_{\text{ink}}}{W_{\text{ink}} + W_{\text{H}_2\text{O}}} \quad (3.1)$$

where  $W_{\text{ink}}$  is the mass of Higgins India ink from the original bottle (7.4237 gr) and  $W_{\text{H}_2\text{O}}$  is the mass of water that was used to dilute the ink. The diluted ink was prepared with reference to a small sample of an existing diluted ink provided to us by the same group who created the ink recipe [Martelli and Zaccanti, 2007]. We started by diluting 7.4237 gr of pure India ink in 1000 gr of di-ionized ultrapure water. Since the recipe was based on the diluted ink from the existing sample, it was important to make sure that the newly prepared ink is comparable to the existing one. To compare the two, samples from both the existing and new ink were each diluted 1:100 in

ultrapure water and placed in a 1 cm plastic cuvette. The absorbance spectra of each sample, as well as the absorbance spectrum of a cuvette containing solely water, were measured in a spectrophotometer (Lambda35, Perkin Elmer) in the 400-850 nm range.

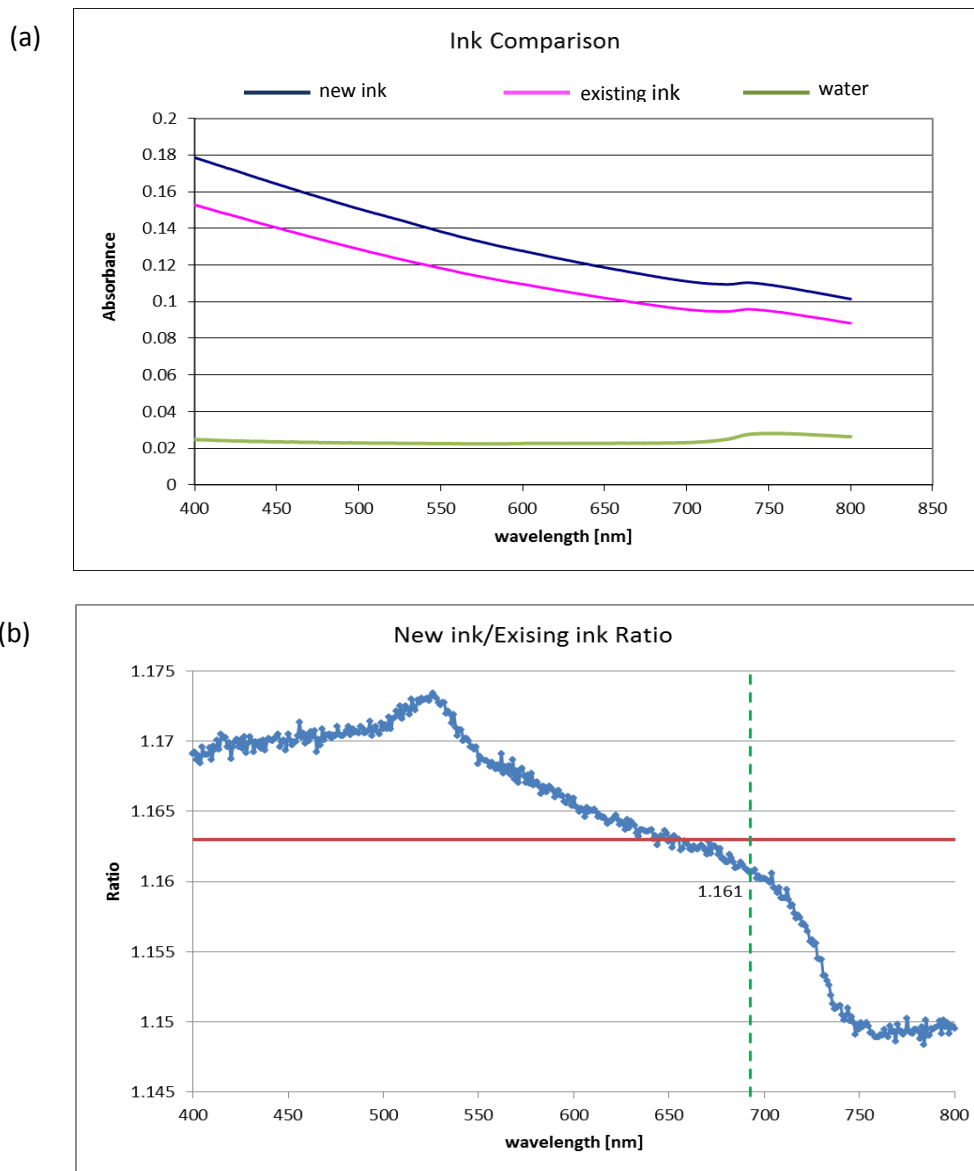


**Figure 3.1** (a) Absorbance spectra of the new ink (blue) and the existing ink (pink). The two samples were diluted in DI water and measured in a spectrophotometer. The reference spectrum of the DI water is in green. The absorbance of the new ink is higher by ~16% compared to the existing ink's absorbance (b).

Figure 3.1-a presents the measured absorbance spectra. The absorbance values (A) were determined according to

$$A = -\log(I/I_0) \quad (3.2)$$

where  $I_0$  and  $I$  are the input and output intensities respectively, and “log” is the base 10 logarithm.

The graph shows a discrepancy between the absorbance of the new and existing ink. To calculate the difference between the two inks, the ratio between the curves was taken and it is presented in figure 3.1-b. The ratio is represented by the blue points, the average ratio is represented by the red line and the dashed green line marks the 690 nm where the ratio is 1.161. The difference between the two samples is such that the new ink is ~ 16% more absorbing than the existing ink. The corrected  $\mu_a$  values (with 16% correction factor) are in the right column of Table 3.1.

In order to calculate the mass of diluted ink ( $W_{\text{ink}}$ ) that is required to achieve a certain  $\mu_a$ , Equation (3.2) was used [Martelli and Zaccanti, 2007]:

$$W_{\text{ink}} = \frac{(\mu_a - \mu_{a\_H2O}) * (W_{H2O\& milk})}{\mu_{t\_ink} * (1 - \Lambda) * \rho_{\text{dilution}} - (\mu_a - \mu_{a\_H2O})} \quad (3.3)$$

where  $\mu_a$  ( $\text{cm}^{-1}$ ) is the desired absorption coefficient of the phantom,  $\mu_{a\_H2O}$  ( $\text{cm}^{-1}$ ) is the absorption coefficient of water,  $W_{H2O\& milk}$  (gr) is the mass of milk-water dilution,  $\mu_{t\_ink}$  ( $\text{cm}^{-1}$ ) is the extinction coefficient (given by  $\mu_a + \mu_s$ ) of the Higgins India ink and  $\Lambda$  is the single scattering albedo of the ink as were measured by Martelli [2007]. The recipe was written to perform calculations for wavelengths 632.8, 750 and 830 nm. Since the wavelength we were using for all

of the experiments was 690 nm, the  $W_{\text{ink}}$  was calculated for 632.8 and 750 nm and then linearly interpolated for 690 nm.

Table 3.1 provides the mass of diluted ink needed to be added to 1000 gr of the milk-water dilution in order to achieve certain absorption coefficients of the medium. The column of 690 nm wavelength contains the interpolated  $W_{\text{ink}}$  values between 632.8 nm and 750 nm.

**Table 3.1** The calculated mass values of diluted ink (existing sample) that are needed to be added to 1000 gr of the milk-water dilution in order to obtain the  $\mu_a$  values in the left column. The column on the right contains the corrected  $\mu_a$  values for using the new ink.

$\lambda$ (nm)	632.8	690	750	Corrected $\mu_a$ (cm <sup>-1</sup> )
$\mu_a$ (cm <sup>-1</sup> )	$W_{\text{ink}}$ (g)	$W_{\text{ink}}$ (g) interpolated	$W_{\text{ink}}$ (g)	
0.03	0.97	0.53	0.10	0.035
0.05	1.68	1.33	0.97	0.058
0.08	2.76	2.52	2.28	0.093
0.10	3.60	3.45	3.30	0.120
0.13	4.49	4.44	4.39	0.149
0.15	5.39	5.44	5.49	0.178

### 3.1.2 Measurement of Optical Properties of the Liquid Phantom

#### 3.2.1.1 Experimental Setup

The scanner and ISS oximeter used in this experiment were the same as the ones used for determining the depth-shift curve in all the other experiments described in this study.

The tips of two 800  $\mu\text{m}$  diameter optic fibers, serving as source and detector, were placed in a tank containing  $\sim 4000$  mL milk-water dilution in an infinite geometry setup (Figure 3.2). The other ends of the fibers were connected to the ISS machine as described in Section 2.1. Only one detector was used in this experiment and it was kept stationary at an initial separation of  $d_0=20$  mm from the source. The source fiber (delivering light at 690 nm) was scanned in a line 30 mm long (up to a source-detector separation of  $d_0=50$  mm). The scanning speed was 10mm/sec and 30 points were collected in each scan. The scan was repeated 4 times for each value of  $\mu_a$ .

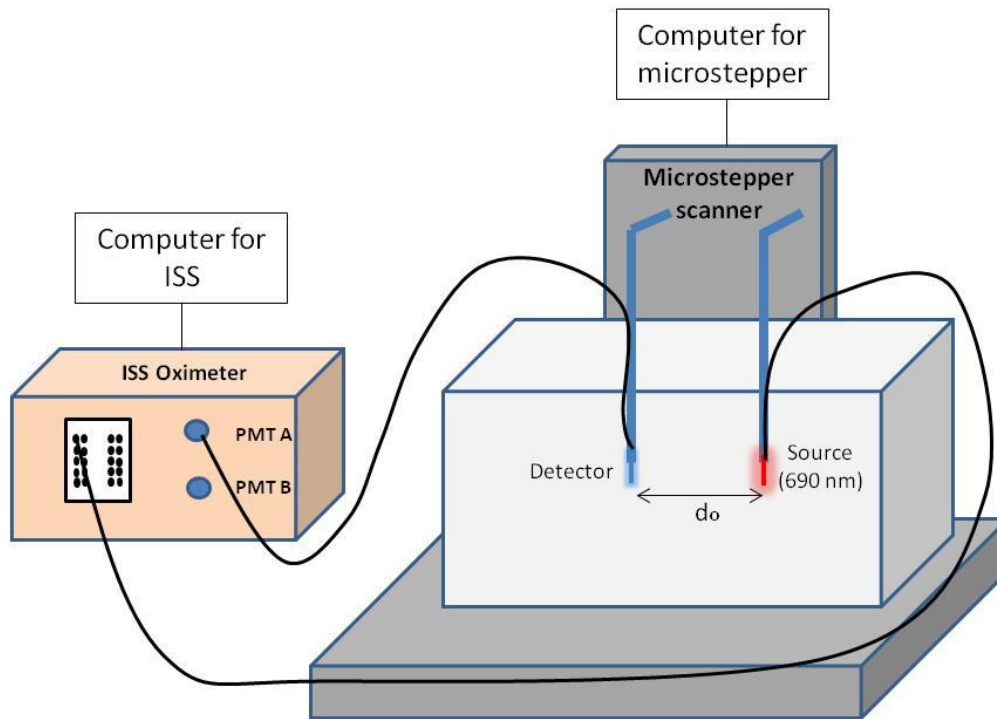


**Figure 3.2** A schematic of the setup used to measure absolute values of  $\mu_a$  and  $\mu_s$  of the liquid phantom. A single detector fiber was fixed in position inside the medium-containing tank. A source fiber (690 nm) was positioned in an initial distance of  $d_0=20$  mm from the detector and scanned up to a distance of  $d_0=50$  mm, collecting 30 data points per scan line.

The experiment started with the milk-water dilution solely and ink was added in increments according to Table 3.1 above (the 690 nm column) to increase the absorption coefficient. The expected  $\mu_a$  values are on the right column. The output file included the AC and phase information of each scan and these were used to calculate the optical properties as described in Section 3.1.2.2 below.

### 3.2.1.2 Data Analysis

The absolute calculations of  $\mu_a$  and  $\mu_{s'}$  of the liquid phantom were done based on the AC and phase information measured by the ISS at each source-detector separation distance [Fantini et al, 1999]. If  $r$  is the source-detector separation (in mm) and the slopes of  $\ln(r*AC)$  and phase as the functions of  $r$  are  $S_{AC}$  and  $S_{\Phi}$  respectively, then the absolute values of  $\mu_a$  and  $\mu_{s'}$  of the infinite medium are given by:

$$\mu_a = \frac{\omega}{2\nu} \left( \frac{S_{\Phi}}{S_{AC}} - \frac{S_{AC}}{S_{\Phi}} \right) \quad (3.4)$$

$$\mu_{s'} = \frac{S_{AC}^2 - S_{\Phi}^2}{3\mu_a} - \mu_a \quad (3.5)$$

where  $\omega$  is the angular modulation frequency of the source intensity and  $\nu$  is the speed of light in the medium.

The calculations of the slopes  $S_{AC}$  and  $S_{\Phi}$  were performed in Matlab by using the recorded photon counts values and the source-detector distances as inputs. The slopes were then used in Equations (3.4) and (3.5) to determine the values of  $\mu_a$  and  $\mu_{s'}$ .

Examples of the linear dependence of  $\ln(r^*AC)$  and phase on the source-detector distance,  $r$  (also referred to as  $d_0$ ), for the cases of  $\mu_a = 0.005 \text{ cm}^{-1}$  and  $\mu_a = 0.093 \text{ cm}^{-1}$  are provided in Figure 3.3 a and b respectively. In both cases the data points were well fitted into a line for accurate slope calculations.

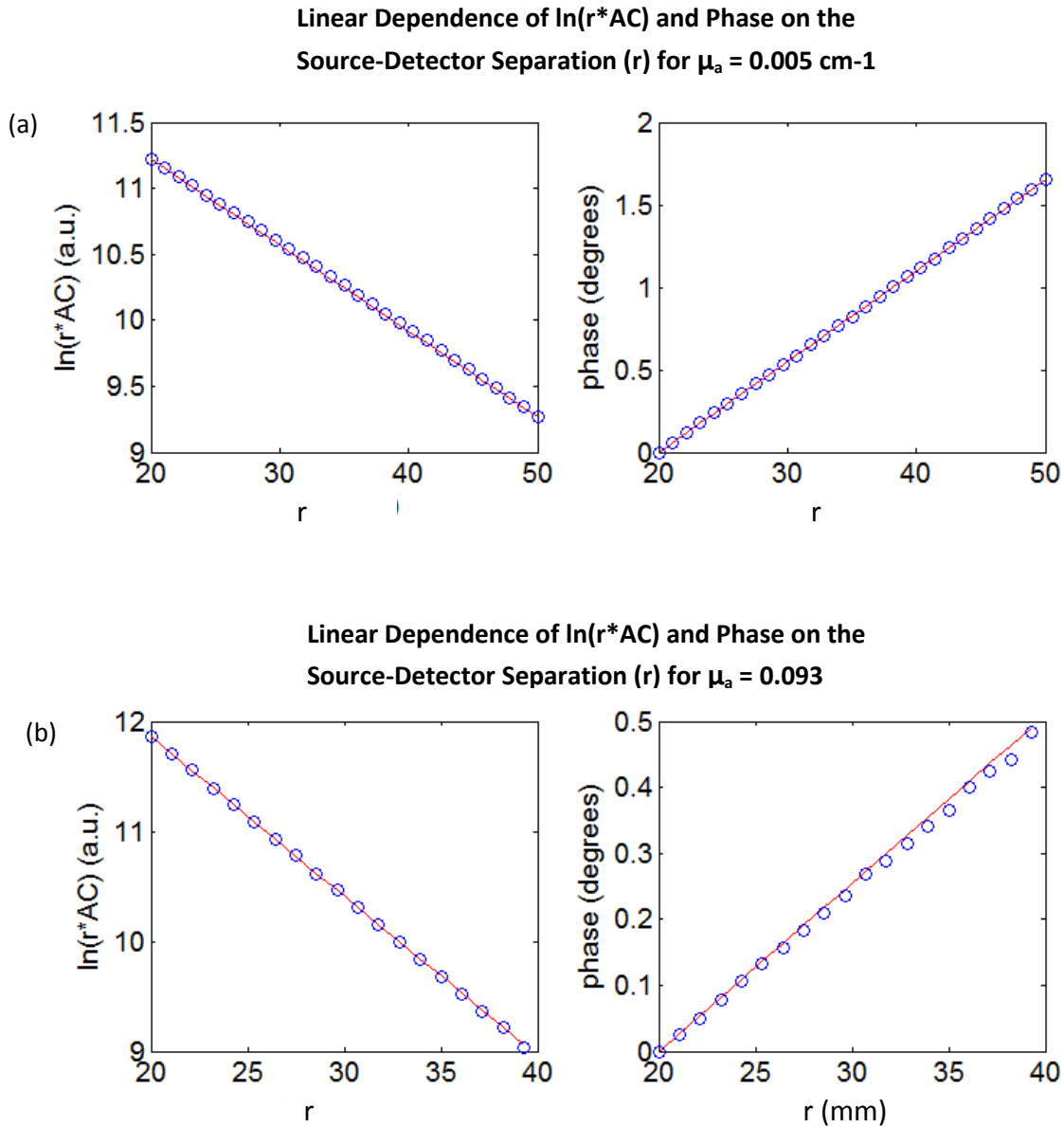


**Figure 3.3** Examples of the linear dependence of  $\ln(r^*AC)$  (left panels) and phase (right panels) on the source-detector distance,  $r$  ( $=d_0$ ), for liquid phantom with  $\mu_a = 0.005 \text{ cm}^{-1}$  (a) and  $\mu_a = 0.093 \text{ cm}^{-1}$  (b).

Figure 3.4 provides a graphical comparison between the measured and expected values of  $\mu_a$  and  $\mu_s$ . Each of the measured values was averaged over four scans and the error is the standard deviation (STD) between the same scans. The expected  $\mu_a$  for the milk-water dilution was  $0.005 \text{ cm}^{-1}$ , similar to  $\mu_a$  of water at 690 nm wavelength [Hale and Querry, 1973]. The  $\mu_s$  of the dilution was expected to be  $\sim 7 \text{ cm}^{-1}$  [Yu et al, 2011] and was assumed to stay consistent over the entire experiment (regardless of the ink concentration).

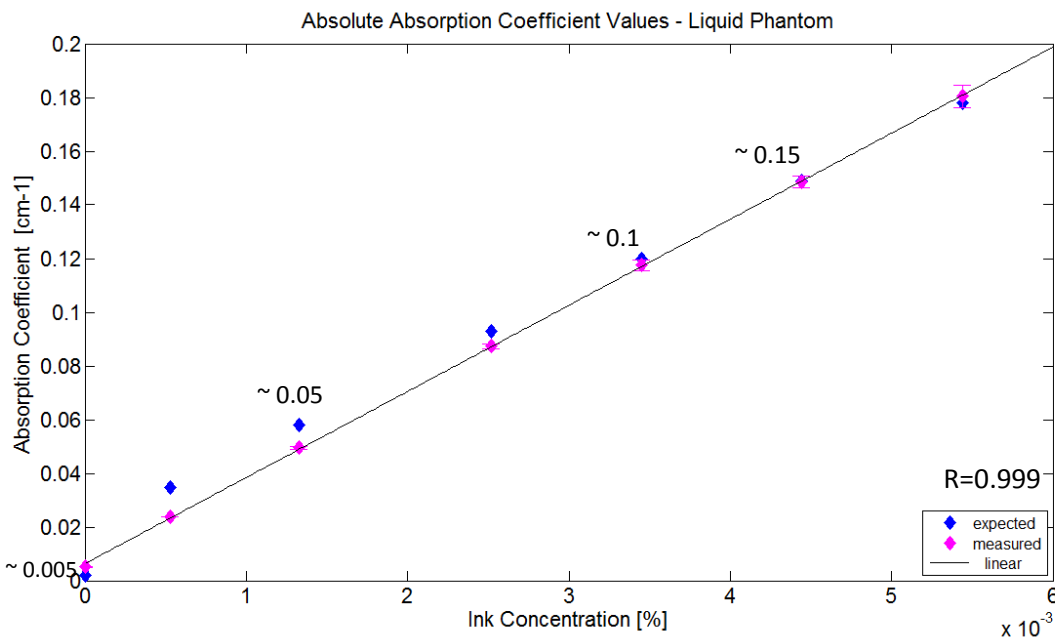


**Figure 3.4** Average absorption coefficient values of the liquid phantom as a function of ink concentration (pink) versus expected values (blue). Error bars are the standard deviation of 4 measurements. Measured values were linearly fitted, demonstrating a linear trend according to the theory and other experimental reports.

It was found that the  $\mu_s$  value stayed consistent across the entire experiment, with an average value of  $7.86 \pm 0.06 \text{ cm}^{-1}$ . This value is in excellent agreement with the reported  $\mu_s$  values for similar liquid phantoms.

The calculated  $\mu_a$  values were in excellent agreement with the expected values reported in the recipe ( $<1\%$  for  $\mu_a$   $0.15 \text{ cm}^{-1}$ ) with the exception of larger errors of  $\sim 45\%$  and  $\sim 20\%$  observed for  $0.035$  and  $0.05 \text{ cm}^{-1}$  respectively. Nevertheless, fitting the data points provided a better linear fit for the measured values ( $R=0.999$ ) than for the expected ones ( $R=0.994$ ), again in excellent agreement with the theory and with other reports in the literature [Fantini et al 1994a], [Fantini et al, 1994b], [Patterson et al, 1991].

In conclusion, the purpose of measuring the absolute optical properties of the liquid phantom was twofold – (1) validating the existing recipe values in our own lab setup, so that future experiments would have a reliable recipe for formulating liquid phantoms; (2) formulating a well-controlled liquid phantom for the depth-shift curve experiments.

### **3.2 Variability of the Depth-Shift Curve**

In order to study the sensitivity of the experimental depth-shift curve to different parameters we performed several experiments where each time, one parameter was changed while the others were fixed. For example, to check the sensitivity of the curve to the sample thickness we performed several scans according to the procedure in Section 2.2 where each scan had a different source-detectors plane separation to achieve various values of  $d_0$ . Table 3.2 provides a summary of the experiments with their different variables. Changing the S-D distance was done by manually sliding the source in the slit in its holder and fixing it in the new distance from the detectors holder. Inclusion size variability was achieved by using different rod sizes. The absorption coefficient of the liquid phantom was changed by adding ink according to the recipe and the protocol presented in Section 3.1. The ink concentration was calculated for a medium volume of 18000 mL. Before each scan where the S-D distance and rod size had to be

adjusted, the liquid in the tank had to be emptied to a level where the rod and source-detectors configuration were visible and approachable. After the S-D distance or the inclusion size were changed the system was realigned the motors were moved to their starting position, keeping the source tip 1 mm from the rod's surface and ~3.5 cm above it (Figure 2.4-a). For the experiment of changing the absorption coefficient the setup had to be aligned only once, at the beginning of the experiment, since adding the ink to the medium did not interfere with the rest of the setup.

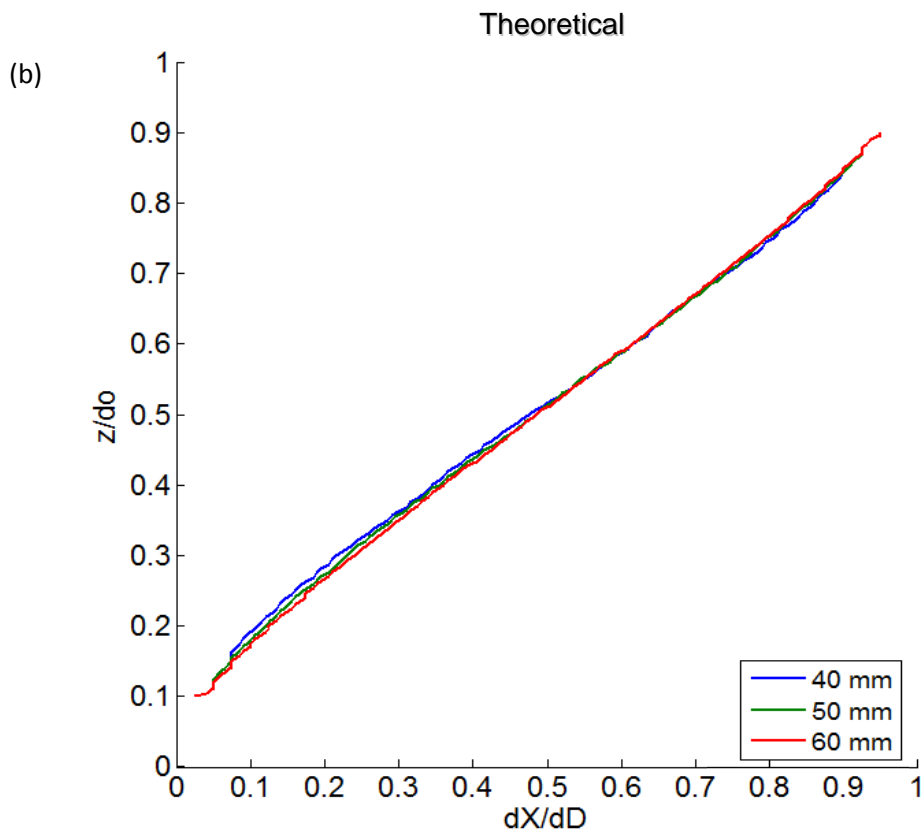
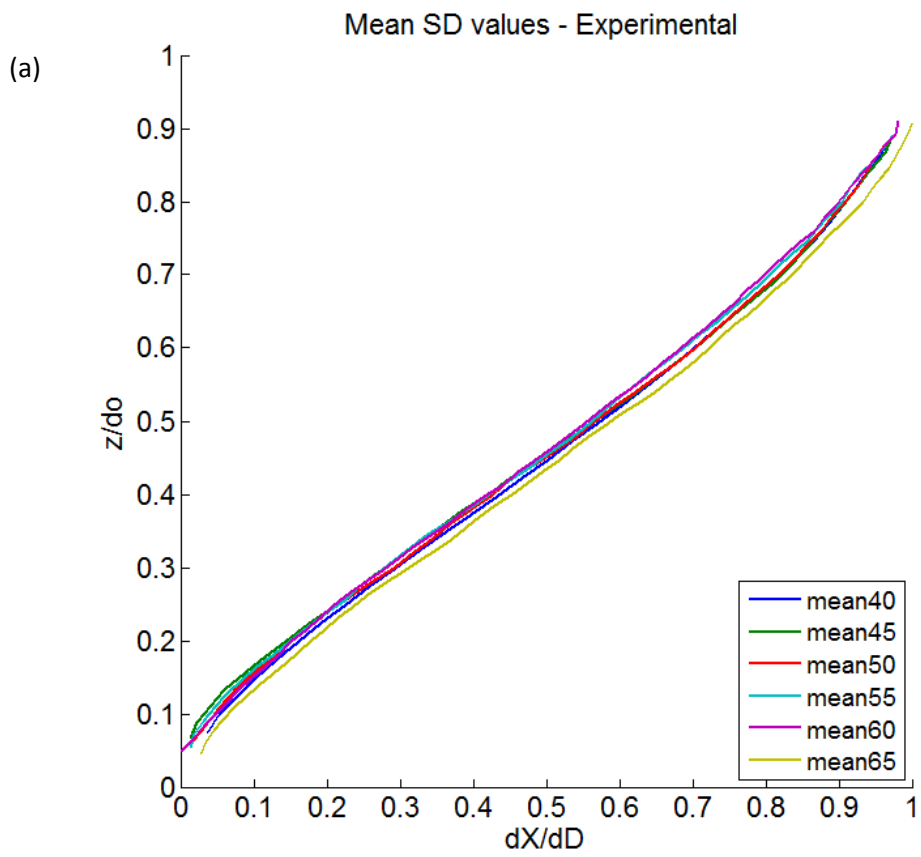
**Table 3.2** A summary table of the variables in each experiment. S-D and D-D refer to source-detectors plane separation and inter-detector separation respectively.  $D_{rod}$  is the rod's diameter and  $\mu_a$  is the absorption coefficient of the liquid phantom. The values of the variable that was changed in each experiment appear in the red-border cells.

Experiment	S-D separation ( $d_0$ ) [mm]	D-D separation ( $\delta D$ ) [mm]	$D_{rod}$ [mm]	$\mu_a$ [ $\text{cm}^{-1}$ ]
Sample thickness	40, 45, 50, 55, 60, 65	19.3	3.5	0.005
Optical properties	40	19.3	3.5	0.005, 0.035, 0.058, 0.093, 0.120, 0.149
Inclusion Size	65	19.3	3.5, 6.5, 12.9	0.005

## Chapter IV - Results

### 4.1 Sensitivity to Sample Thickness

Figure 4.1 shows the depth-shifts curves obtained for different S-D values: experimental (a), theoretical (b) and the overlay of experimental and theoretical curves (c). The theoretical curves were determined with parameters similar to the experimental setup – infinite geometry, medium optical properties  $\mu_a = 0.005 \text{ cm}^{-1}$  and  $\mu_s' = 8 \text{ cm}^{-1}$ , rod with 3.5 mm diameter as the inclusion, D-D distance of 20 mm and S-D distances of 40, 50 and 60 mm. As reported by Grosenick et al [2004] and Kainerstorfer et al [2013] for point-like and spherical inclusions, the theoretical depth-shift curve for the cylindrical inclusion is weakly sensitive to variations in sample thickness. The experimental curves (Figure 4.1-a) are the average curves over multiple measurements. For S-D distance of 40 and 65 mm the curve was averaged over 4 independent measurements. The rest of the curves were averaged over 2 independent measurements. Here we define independent measurements as being conducted after the setup was realigned (contrary to repeating a scan with simply restarting the motors and without having to readjust the setup). The error bars in Figure 4.1-c are based on the standard deviation of the 4 independent measurements for S-D distance of 40 mm. As can be seen in Figure 4.1-b, the experimental curve is insensitive to variations in sample thickness, consistent with the theoretical model. The overlaying of the theoretical and experimental results reveals a discrepancy between the curves that is translated into maximal errors of 3 and 6 mm in depth for S-D 40 mm and 65 mm respectively.



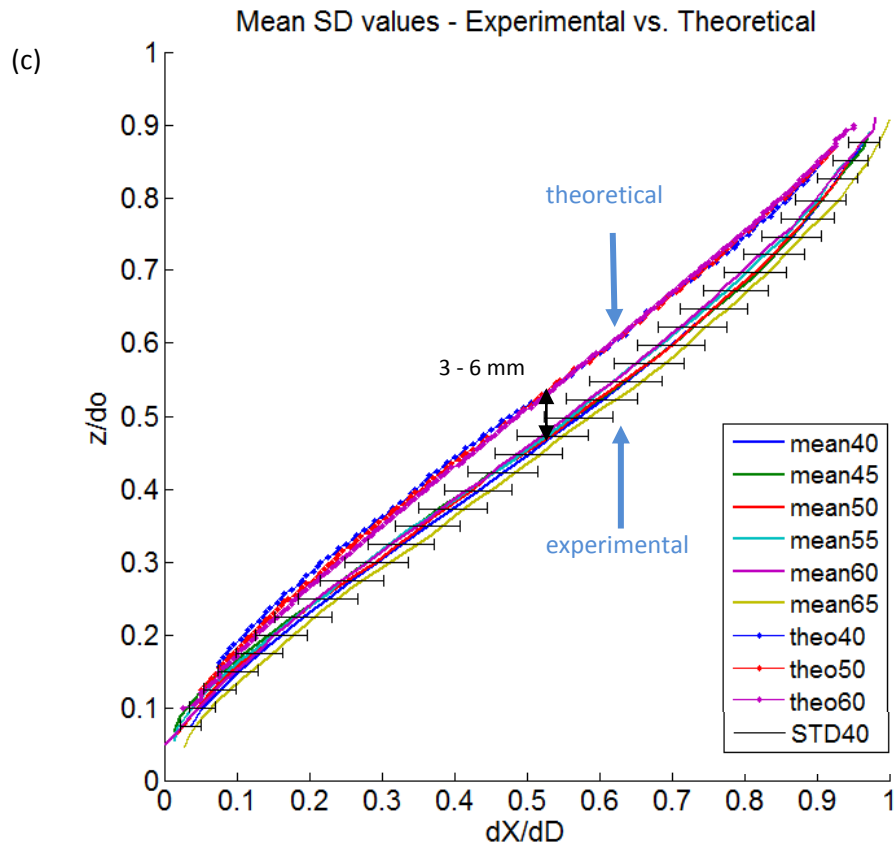


**Figure 4.1** (a) Measured depth-shift curves for different sample thickness, their corresponding theoretical curves (b) and the overlay of both (c). The experimental curve demonstrates insensitivity to sample thickness consistent with the behavior of the theoretical curve. The overlay shows a discrepancy in the range of 3-6 mm.

The discrepancy is minimal when the perturbation is closer to the source and increases to its maximum when the perturbation is around the midpoint (i.e. the point having coordinates  $(dx/dD, z/d0)=(0.5, 0.5)$ ) between the source and the detectors plane. These discrepancies will be addressed in the Discussion section.

As part of our work we were also interested in using the experimental depth-shift curve to obtain the depth of an inclusion from past experiments [Kainerstorfer et al, 2013]. The same system

and setup described here were used for scanning the liquid phantom containing 6 different black rods that were positioned in different depths between the source and detectors. Since this scan was performed several months before we measured the experimental depth-shift curve, it was interesting to both test the reproducibility of the system and compare measured depths obtained by the experimental curve versus the theoretical model. Since the scan was performed for S-D distance of 65 mm with  $\mu_a = 0.005 \text{ cm}^{-1}$ ,  $\mu_s = 8 \text{ cm}^{-1}$  and 3.5 mm diameter black rods, we used our averaged curve named “mean65” from Figure 4.1 above and the corresponding theoretical curve. The measured depths were compared to actual depth values and they are presented in Figure 4.2.

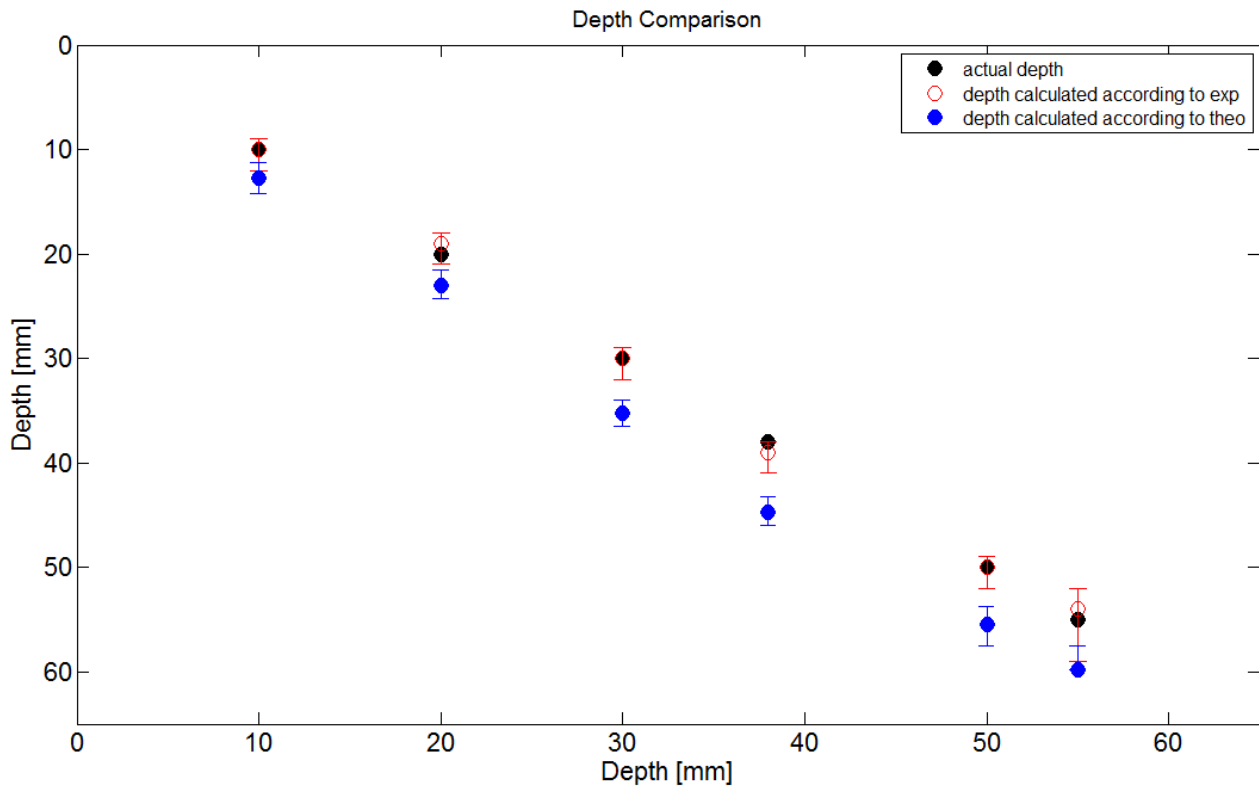


**Figure 4.2** Measured depth of 6 rod inclusions (solid black circles) according to the experimental depth-shift curve (open red circles) and the theoretical depth-shift curve (solid blue circles). The error bars were plotted for uncertainty of 1 pixel (0.5 mm)

Actual depths appear in solid black circle, measured depths according to the theoretical model are in solid blue circles and depths measured according to the experimental curve are in open red circles. The error bars were plotted for an uncertainty of 1 pixel (0.5 mm) in  $\delta x$  measurements for both curves. The comparison above shows that depths that were measured with the experimental curve are in excellent agreement with the actual depth values, with a maximal error of 1 mm. This supports the robustness of our setup and the reproducibility of the measurements. Depth measurements according to the theoretical model had a larger error ranging from  $\sim 3$  mm close to the source and  $\sim 6$  mm towards the midpoint and on, supporting the observed behavior of the discrepancy between experimental and theoretical curves (smaller error close to the source and larger error towards the midpoint). This behavior will be referred to in the Discussion section.

#### **4.2 Sensitivity to Background Optical Properties**

Figure 4.3 presents the theoretical and experimental depth-shift curves for different  $\mu_a$  values. The theoretical model (Figure 4.3-b) demonstrates that for absorption coefficients of  $0.058 \text{ cm}^{-1}$  and higher the curve is weakly sensitive to variations in  $\mu_a$  with a maximal discrepancy of  $\sim 0.5$  mm for S-D of 40 mm. For lower absorptions the discrepancy was found to be  $\sim 1.5$  mm. Regardless of these variations, the theoretical curves are characterized by passing through the midpoint, half way between the source and the detectors, thus the discrepancy between them is bigger when the perturbation is closer to the source/detectors and minimal in the middle.

The experimental curves presented here (Figure 4.3-a) are the averages between the curves obtained in two separate experiments conducted one week apart. The same behavior and trend

was demonstrated in both experiments. The experimental curves show a trend in their variation, which is clearly dependent on the absorption coefficient. Unlike the previous experiment (Section 4.1), where we adjusted the S-D distance before each scan, thereby increasing the chance for an error in measurement, here the setup was fixed and the only difference between the scans was the addition of ink to the liquid phantom. Therefore, we cannot relate the trend in the curves' behavior to a measurement error or to misalignment between the scans. The discrepancy between the theoretical and the experimental curves is visible mainly at the lowest absorption of the medium. In fact we note that when we consider the three highest absorptions of the background medium the curves are within the same error. As an example, we overlaid only the depth-shift curve obtained for  $\mu_a$  of  $0.149 \text{ cm}^{-1}$  with its corresponding theoretical curve (Figure 4.3-d). The curves show a very good agreement with a slightly higher discrepancy closer to the source ( $\sim 1 \text{ mm}$ ). The overlay of the depth-shift curve obtained for  $\mu_a$  of  $0.005 \text{ cm}^{-1}$  curves (Figure 4.2-e) shows that the theoretical curve falls outside of the experimental curve's error bars; however the maximal discrepancy between them is  $< 3 \text{ mm}$ .

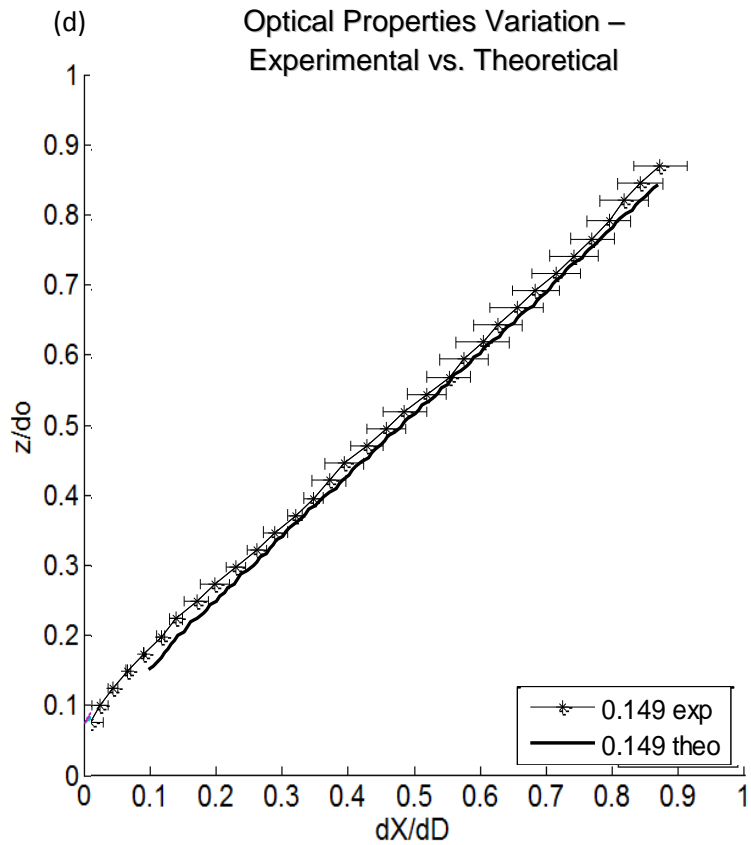
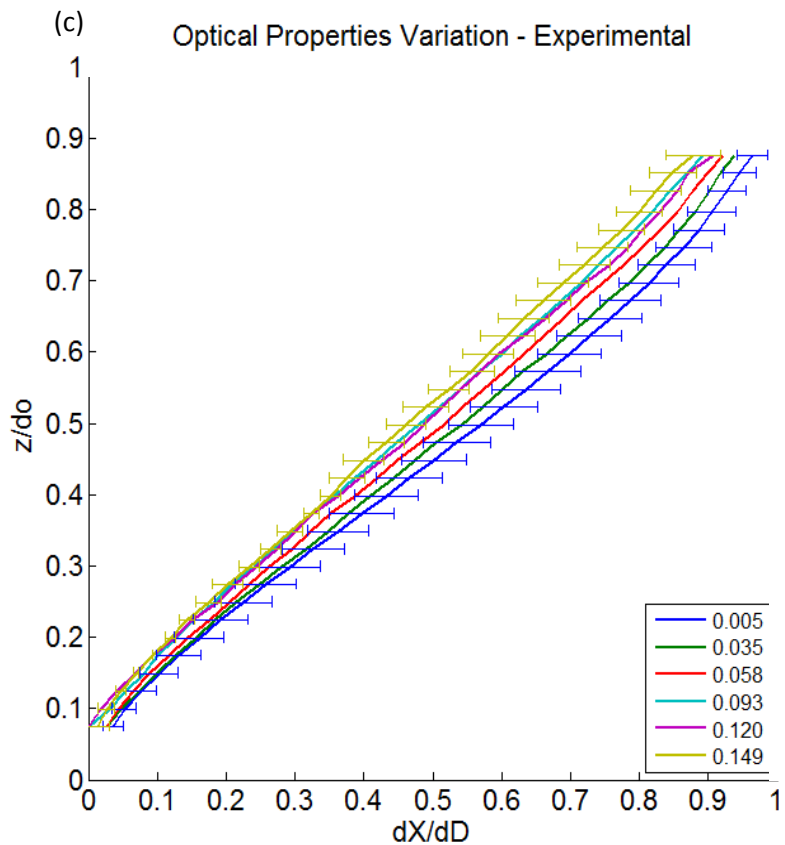
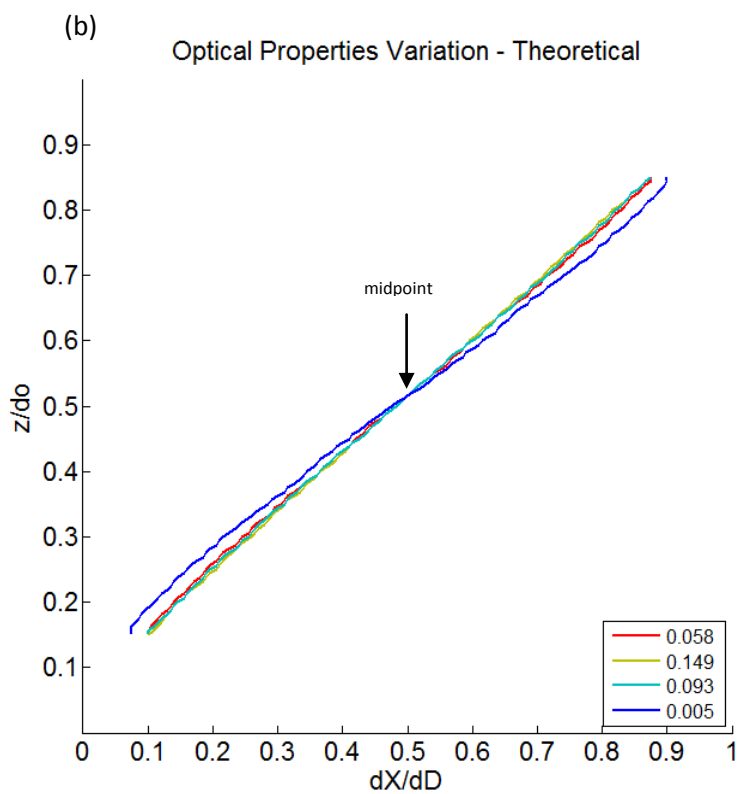
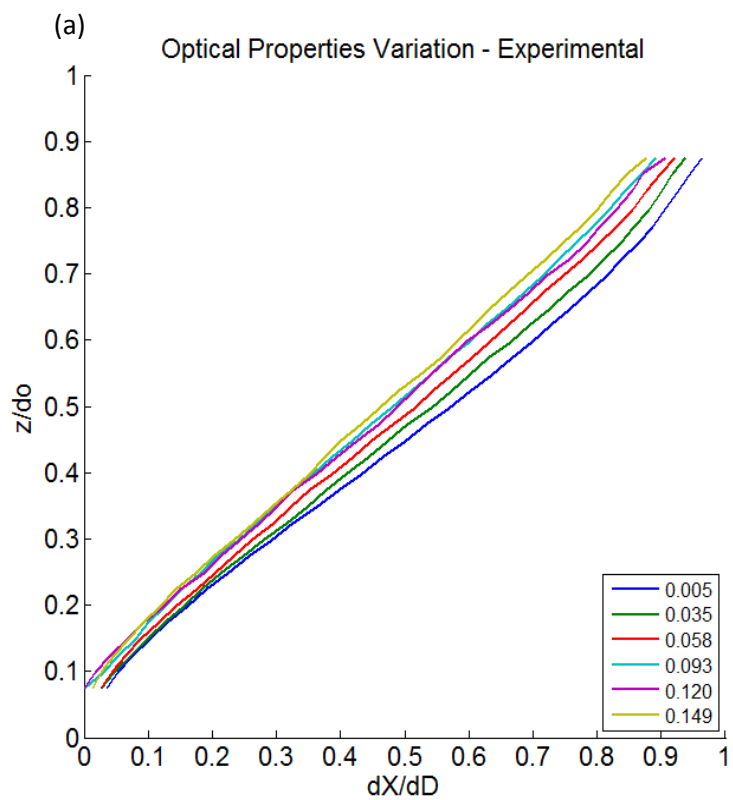
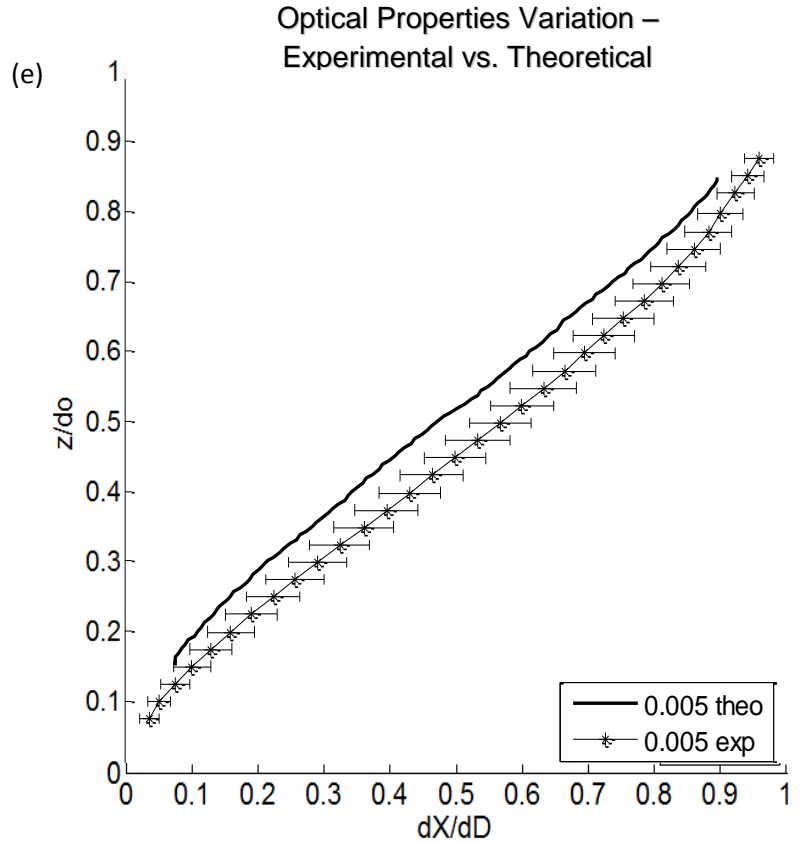


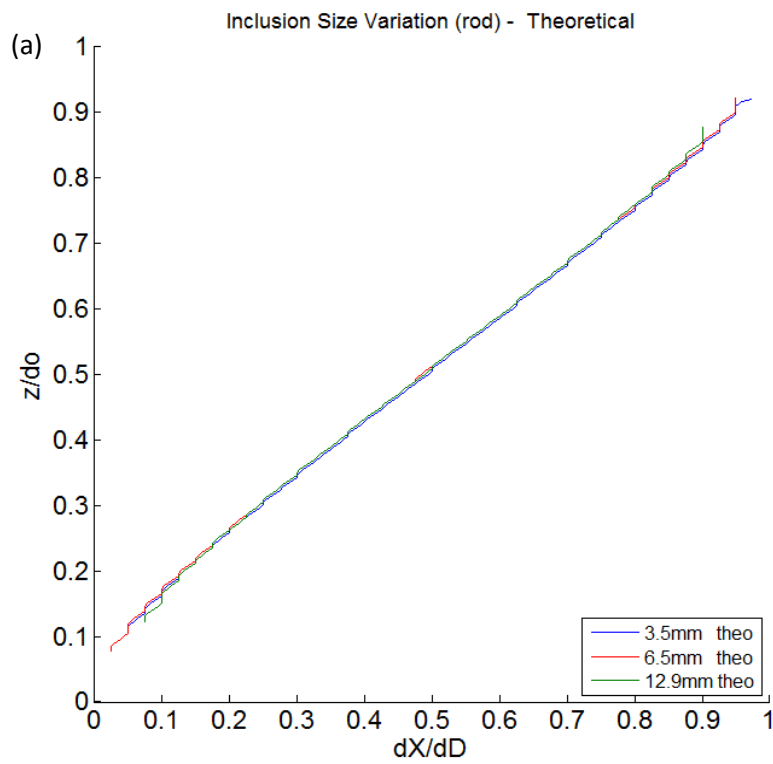
**Figure 4.3** Average experimental depth-shift curves measured for variation in background optical properties without and with error bars (a) and (c) respectively. Corresponding theoretical depth-shift curves for  $\mu_a$  values of 0.005, 0.058, 0.093 and 0.149  $\text{cm}^{-1}$  (b). Overlay of experimental and theoretical curves for  $\mu_a$  of 0.149  $\text{cm}^{-1}$  (d) and 0.005  $\text{cm}^{-1}$  (e). The overlay for the higher absorption curves shows a very good agreement of the experimental curve with the theoretical model. The overlay of lowest absorption curves shows a discrepancy which, however is  $< 3$  mm.



### 4.3 Sensitivity to Inclusion Size

Figure 4.4 includes the theoretical (a), experimental (b) and the overlay (c) of depth-shift curves for three different inclusions having diameter of 3.5, 6.5 and 12.9 mm. Both the theoretical model and the experimental results show that the depth-shift curve is not sensitive to the inclusion size, thus the experimental curve confirms the behavior of the theoretical model. The overlay of the theoretical and experimental curves show a discrepancy which is minimal ( $\sim 1.5$  mm) when the perturbation is close to the source and maximal ( $\sim 7$  mm) around the midpoint. The error bars are the standard deviation of four independent measurements for  $D_{\text{rod}} 3.5$  mm. These results follow the trend we saw in the previous experiments in the sense that the error is

minimal closer to the source, demonstrating the consistency of the error across the different experiments. Similar to the experiment of optical properties variation, the alignment in this experiment was fixed once and was not readjusted between the scans. The only difference between the scans was changing the rods and moving the source tip to keep a distance of 1 mm away and 35 mm above the rod's surface.



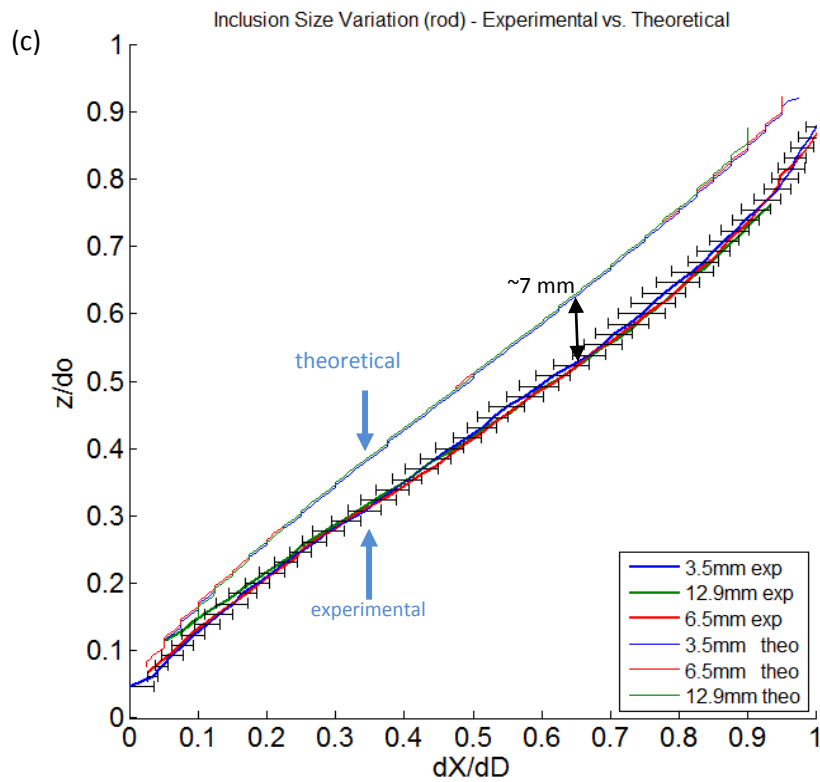
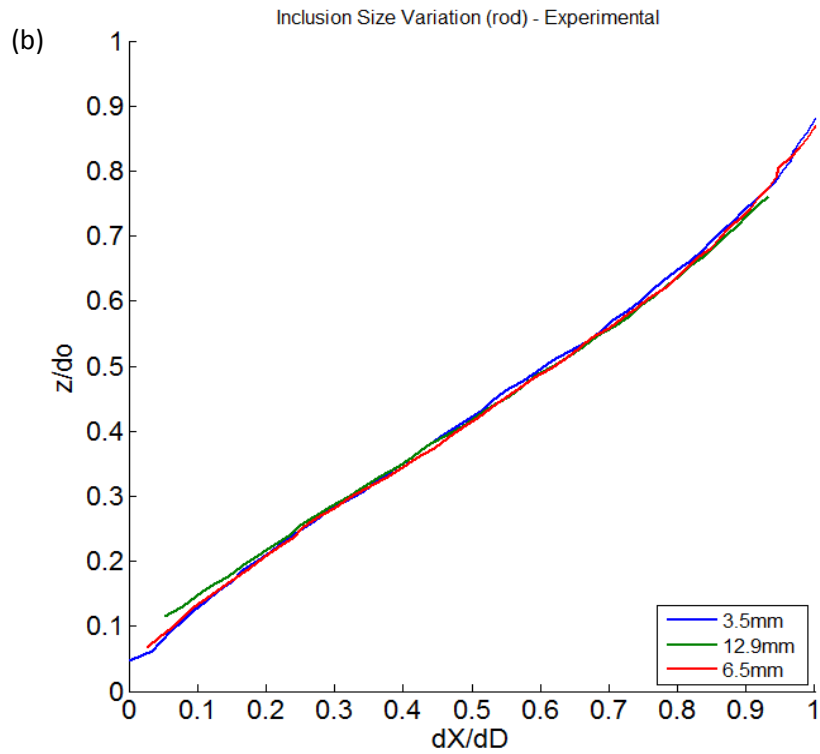


**Figure 4.4** Depth-shift curves for different rod diameters of 3.5, 6.5 and 12.9 mm – theoretical model (a), experimental results (b) and their overlay (c). Both experimental and theoretical curves show insensitivity to inclusion size. The overlay figure shows a maximal discrepancy of  $\sim 7$  mm.

## Chapter V – Discussion and Conclusions

### 5.1 Discussion

Using 2D planar scanning to perform diffuse optical imaging of the breast offers the advantage of increased spatial resolution in the x-y plane of the image space. Depth information can be added to the image by using a second off-axis detector and relating the spatial shift of an inhomogeneity between the images of two detectors to its depth in the sample. The off-axis shifts are related to the depth by a theoretical depth-shift curve, based on diffusion theory. Theoretical results in two typical geometries used in diffusion theory, the slab and the infinite geometry have shown that the differences in the depth-shift curves are within 4%, which yield a maximum discrepancy in the estimated depth of ~1.5 mm for typical source-detector separations. The importance of these results is that in principle, and for practical situations, we could use one “universal” depth-shift curve obtained from the theory under certain conditions which are typical for optical mammography (e.g. typical source-detector separation, optical properties, etc.). However we don’t know how these ideal conditions assumed by the theory (from which the depth-shift curves are derived) can be met in an actual experiment. For example it is well known that diffusion theory becomes less accurate when the photons of interest (in the case of the present study those photons that are absorbed by the inclusions) underwent only few scattering events from the emission point. Moreover the theory cannot incorporate exact boundary conditions especially those involving three media like in a real experiment (where the media are: the tissue, the polycarbonate plates and air). Therefore, the focus of our work was to measure the depth-shift curves through a series of experiments in the simplest geometry, i.e. the infinite medium geometry (where the boundary conditions are not considered), each time varying a

certain parameter while fixing the others, and comparing these curves to the corresponding theoretical ones.

The parameters that were varied during the different experiments were: the sample thickness, the background optical properties and the inclusion size. For the experiments conducted by varying the sample thickness and the inclusion size we found that the experimental and the theoretical curves shared the same behavior, i.e. they are rather insensitive to changes in these variables. However, an absolute comparison between the theoretical and experimental curves revealed a discrepancy of up to 7 mm in the estimated depths. In the experiments where the optical properties of the medium were varied we found that the experimental depth-shift curve was partially consistent with the theoretical model. For higher absorption coefficient values ( $> 0.09 \text{ cm}^{-1}$ ) there was a very good agreement with the theoretical model both in terms of the behavior of the curves and the absolute comparison. Larger discrepancies were found between curves with lower absorption values and this finding is consistent with the discrepancies observed in the results of other two experiments (sample thickness and inclusion size variation) which were also conducted with low absorption value of the medium ( $0.005 \text{ cm}^{-1}$ ).

As was described earlier, the shape of the depth-shift curve is determined by the shape of the light bundle, which is the region visited by the photons on their propagation from the light source to the optical detector in the medium (depicted in Figure 1.4). Therefore, only factors that affect the shape of the light bundle could affect the shape of the depth-shift curve and cause for discrepancies between the theoretical and experimental curves. For example, while the theoretical model assumes an isotropic point source, in the experimental setup the source was not isotropic and resulted in a spatially distributed light source in front of the illumination fiber that can affect the shape of the light bundle. In addition, the bulky apparatus (posts and fiber holders)

that was immersed inside the medium could affect the shape of the light bundle if it was acting as a reflector or diffuser as opposed to a complete absorber of light. Although the apparatus was covered with black tape to avoid such a case, we cannot be sure that it acted as a pure absorber and therefore it could have contributed to the discrepancy from the model, especially for curves that were measured with low absorption values where the photons have a higher chance of being incident on the apparatus. More generally, the details of the experimental boundary conditions (walls of container, free surface of liquid medium, mechanical mounts to hold fibers, etc.) may also account for effects on the shape of the light bundle that are not included in the theoretical calculations.

The above possible sources of discrepancy were expected to cause larger errors when the inclusion is located closer to the boundaries, i.e source, and in fact this was observed in curves that were measured with background absorption coefficient  $> 0.09 \text{ cm}^{-1}$ . However, most of our results (measured for  $\mu_a=0.005 \text{ cm}^{-1}$ ) demonstrate that the maximal discrepancy with respect to the theoretical model is when the inclusion is located towards the midpoint between source and detectors plane. We speculate that this is due to the effect of boundary conditions which is more dominant for lower absorption values of the medium where the optically probed volume becomes larger. Further investigation is required to understand the sources of error and the reason why maximal discrepancies were typically found towards the midpoint.

The observation that the experimental depth-shift curve demonstrated a different behavior for background absorption coefficient values that were higher and lower than  $0.09 \text{ cm}^{-1}$  suggests that the depth-shift curve would also be dependent on the light wavelength. For example, if we consider typical chromophore concentrations of the breast as reported by Svensson [2005] (Figure 5.1) we can expect a smaller sensitivity of the curve to variations in  $\mu_a$  by using a light

source emitting at wavelengths  $> \sim 880\text{nm}$  or  $< \sim 630\text{nm}$  where the total  $\mu_a$  of the breast is larger than  $0.09\text{ cm}^{-1}$ .

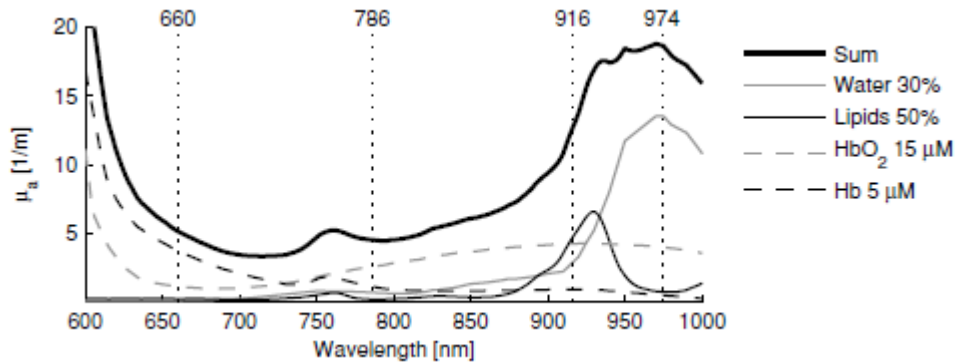


**Figure 5.1** Typical absorption spectra of breast tissue. Vertical dotted lines represent the positions of diode lasers. [Svensson et al, 2005]

The ultimate goal of the proposed depth assessment method would be to assess the location of tumors within the breast, considering localization is regarded as key in surgical planning for breast conservation. A precise localization of breast tumor is vital for guiding the surgeon to the lesion site, and ascertaining its correct and adequate removal with satisfactory excision margins. A well established localization method is the hook wire localization, which is performed following multiple x-ray mammograms, or guided by ultrasound, to help pinpoint the location of the tumor. Together with the fact that it is invasive, this method has several other drawbacks, i.e the wire could stray during its navigation, thus making it hard to locate the lesion; oftentimes the wire entry site is distant from the tumor which could have a cosmetic effect [Kass et al, 2007]. Assuming that the proposed depth assessment method of this study could be implemented on the optical mammography system thereby allowing for depth measurements of breast tumors, it could be used as a non-invasive real time localization tool for biopsy

procedures. Moreover, the assessment of spatial position of blood vessels could be helpful in relating blood vasculature to the location of tumors, given the relevance of blood supply and blood drainage to and from the tumor, thereby providing valuable information for surgical planning of tumor excision. Lastly, depth information acquired by the optical mammography scanner could be used as apriori information for improving 3D spatial reconstruction of diffuse optical tomography data.

## **5.2 Conclusions**

The aim of this project was to test if the ideal conditions used by the theoretical model to derive the depth-shift curves are met in an experimental situation in the simplest geometry of the medium. Specifically, we wanted to compare the experimental and the theoretical depth-shift curves to variations in sample thickness, background optical properties, and inclusion size in the infinite geometry medium for a cylindrical inclusion. After measuring the curve for the different variables we found that the experimental depth-shift curve is insensitive to variations in sample thickness and inclusion size, consistent with the theoretical model. Nevertheless, absolute discrepancies of several millimeters between the theoretically and experimentally assessed depths were found. We argued that these discrepancies are possibly due to a combination of realistic conditions that were different from the ideal conditions of the model, for example the spatial distribution of the light source, the effect of the experimental apparatus and boundary conditions introduced by the liquid phantom. In the experiments where the background optical properties were varied the experimental results showed a very good agreement with the theory for absorption coefficient values  $> 0.09 \text{ cm}^{-1}$ , both in the behavior of the curves and in the

absolute comparisons. This finding reinforces our conviction that at lower absorption values (which were used in all the other experiments) boundary conditions had a noticeable effect on the measured depth-shift curve. Further investigation is required to explain absolute discrepancies between the theoretical model and experimental results for lower absorption values of the medium, specifically the larger errors when the perturbation is located at the midpoint between source and detectors.

### **5.3 Future Steps**

Several questions remain as to the behavior of the experimental depth-shift curve and its variation from the theory. One issue that needs to be addressed is the bulky apparatus that was used to position the source and detector fibers inside the medium. Protruding the source fiber further away from its holder could help minimize boundary effects when the inclusion is close to the source. A more ideal solution would be to have only the fibers themselves submerged inside the medium such that any device holding them is not included in the phantom. In addition, since the ultimate goal of this study is to implement depth assessment capabilities in our optical mammography scanner, experimental depth curves should be derived for this instrument and for typical breast tissue parameters.

## References

- Arridge, S. R. and W. R. B. Lionheart (1998). "Nonuniqueness in diffusion-based optical tomography." *Opt. Lett.* 23(11): 882-884.
- Cheong, W. F., S. A. Prahl, et al. (1990). "A review of the optical properties of biological tissues." *Quantum Electronics, IEEE Journal of* 26(12): 2166-2185.
- Choe, R., S. D. Konecky, et al. (2009). "Differentiation of benign and malignant breast tumors by in-vivo three-dimensional parallel-plate diffuse optical tomography." *J Biomed Opt* 14(2): 3103325.
- Cyrlak, D. (1988). "Induced costs of low-cost screening mammography." *Radiology* 168(3): 661-663.
- Dehghani, H., S. Srinivasan, et al. (2009). "Numerical modelling and image reconstruction in diffuse optical tomography." *Philos Transact A Math Phys Eng Sci* 367(1900): 3073-3093.
- Durduran, T., R. Choe, et al. (2002). "Bulk optical properties of healthy female breast tissue." *Phys Med Biol* 47(16): 2847-2861.
- Enfield, L. C., A. P. Gibson, et al. (2007). "Three-dimensional time-resolved optical mammography of the uncompressed breast." *Appl Opt* 46(17): 3628-3638.
- Fantini, S., M. A. Franceschini, et al. (1994). "Quantitative determination of the absorption spectra of chromophores in strongly scattering media: a light-emitting-diode based technique." *Appl Opt* 33(22): 5204-5213.
- Fantini, S., S. A. Walker, et al. (1998). "Assessment of the size, position, and optical properties of breast tumors in vivo by noninvasive optical methods." *Appl Opt* 37(10): 1982-1989.
- Fantini, S., M. Franceschini, et al. (1999). "Non-invasive optical mapping of the piglet brain in real time." *Opt Express* 4(8): 308-314.
- Fantini, S. and A. Sassaroli (2012). "Near-infrared optical mammography for breast cancer detection with intrinsic contrast." *Ann Biomed Eng* 40(2): 398-407.
- Grosenick, D., K. T. Moesta, et al. (2003). "Time-domain optical mammography: initial clinical results on detection and characterization of breast tumors." *Appl Opt* 42(16): 3170-3186.
- Grosenick, D., H. Wabnitz, et al. (2004). "Concentration and oxygen saturation of haemoglobin of 50 breast tumours determined by time-domain optical mammography." *Phys Med Biol* 49(7): 1165-1181.
- Grosenick, D., H. Wabnitz, et al. (2005). "Time-domain scanning optical mammography: II. Optical properties and tissue parameters of 87 carcinomas." *Phys Med Biol* 50(11): 2451-2468.

- Hale, G. M. and M. R. Querry (1973). "Optical Constants of Water in the 200-nm to 200-microm Wavelength Region." *Appl Opt* 12(3): 555-563.
- Hubbard, R. A., K. Kerlikowske, et al. (2011). "Cumulative probability of false-positive recall or biopsy recommendation after 10 years of screening mammography: a cohort study." *Ann Intern Med* 155(8): 481-492.
- Jacques, S. L., S.A Prah1 (1998). "Reduced Scattering Coefficient." Web. <<http://omlc.ogi.edu/education/ece532/class3/musp.html>>
- Jacques, S. L. and B. W. Pogue (2008). "Tutorial on diffuse light transport." *Journal of Biomedical Optics* 13(4): 041302-041302.
- Jemal, A., M. M. Center, et al. (2010). "Global patterns of cancer incidence and mortality rates and trends." *Cancer Epidemiol Biomarkers Prev* 19(8): 1893-1907.
- Kainerstorfer, J. M., Y. Yu, et al. (2013). "Depth Discrimination in Diffuse Optical Transmission Imaging by Planar Scanning Off-Axis Fibers: INITIAL Applications to Optical Mammography." *PLoS One* 8(3): 14.
- Kass R. B., S. D. Lind, et al. (2007). "Breast Procedures." *ACA Surgery, Principles & Practice*. Chapter 3 (Breast, skin and soft tissue), Section 5.
- Martelli, F. and G. Zaccanti (2007). "Calibration of scattering and absorption properties of a liquid diffusive medium at NIR wavelengths. CW method." *Opt Express* 15(2): 486-500.
- Ntziachristos, V., A. G. Yodh, et al. (2002). "MRI-guided diffuse optical spectroscopy of malignant and benign breast lesions." *Neoplasia* 4(4): 347-354.
- Patterson, M. S., J. D. Moulton, et al. (1991). "Frequency-domain reflectance for the determination of the scattering and absorption properties of tissue." *Appl Opt* 30(31): 4474-4476.
- Pogue, B. W., S. C. Davis, et al. (2006). "Image analysis methods for diffuse optical tomography." *J Biomed Opt* 11(3): 33001.
- Ries LAG, M.D., M. Krapcho, et al. (2007). "SEER Cancer Statistics Review, 1975-2004." National Cancer Institute.
- Schmitz, C. H., D. P. Klemer, et al. (2005). "Design and implementation of dynamic near-infrared optical tomographic imaging instrumentation for simultaneous dual-breast measurements." *Appl Opt* 44(11): 2140-2153.
- Shah, N., A. Cerussi, et al. (2001). "Noninvasive functional optical spectroscopy of human breast tissue." *Proc Natl Acad Sci U S A* 98(8): 4420-4425.
- Svensson, T. J. Swartling et al. (2005). "Characterization of normal breast tissue heterogeneity using time-resolved near-infrared spectroscopy". *Phys. Med. Biol.* 50: 2559–2571

- Taroni, P., A. Pifferi, et al. (2003). "In vivo absorption and scattering spectroscopy of biological tissues." *Photochem Photobiol Sci* 2(2): 124-129.
- Tromberg, B. J., O. Coquoz, et al. (1997). "Non-invasive measurements of breast tissue optical properties using frequency-domain photon migration." *Philos Trans R Soc Lond B Biol Sci* 352(1354): 661-668.
- Yu, Y., N. Liu, et al. (2009). "Near-infrared spectral imaging of the female breast for quantitative oximetry in optical mammography." *Appl Opt* 48(10): D225-235.
- Yu, Y., A. Sassaroli, et al. (2010). "Near-infrared, broad-band spectral imaging of the human breast for quantitative oximetry: Applications to healthy and cancerous breasts." *Journal of Innovative Optical Health Sciences* 03(04): 267-277.
- Yu, Y. (2011). "Diffuse Optical Imaging and Spectroscopy of the Human Breast for Quantitative Oximetry with Depth Resolution." Tufts University. Dissertations and Theses.
- Van Steen, A. and R. Van Tiggelen (2007). "Short history of mammography: a Belgian perspective." *Jbr Btr* 90(3): 151-153.
- Weliwitigoda, G. (2012). "Depth Discrimination of Optical Inhomogeneities in a Liquid Phantom using a 2D Planar Scanning Diffuse Optical Imaging System." Tufts University. Dissertations and Theses.
- 3D Advanced Lessons. Volume Rendering for Artists. Web. <<http://www.scratchapixel.com>.>